

Perovskite Materials for Light-Emitting Diodes and Lasers

Veldhuis, Sjoerd Antonius; Boix, Pablo P.; Yantara, Natalia; Li, Mingjie; Sum, Tze Chien; Mathews, Nripan; Mhaisalkar, Subodh Gautam

2016

Veldhuis, S. A., Boix, P. P., Yantara, N., Li, M., Sum, T. C., Mathews, N., et al. (2016). Perovskite Materials for Light-Emitting Diodes and Lasers. *Advanced Materials*, 28(32), 6804-6834.

<https://hdl.handle.net/10356/83316>

<https://doi.org/10.1002/adma.201600669>

© 2016 Wiley-VCH Verlag GmbH & Co. KGaA, Weinheim. This is the author created version of a work that has been peer reviewed and accepted for publication by *Advanced Materials*, Wiley-VCH Verlag GmbH & Co. KGaA, Weinheim. It incorporates referee's comments but changes resulting from the publishing process, such as copyediting, structural formatting, may not be reflected in this document. The published version is available at: [<http://dx.doi.org/10.1002/adma.201600669>].

Downloaded on 09 Apr 2024 12:19:06 SGT

Perovskite Materials for Light Emitting Diodes and Lasers

By Sjoerd A. Veldhuis^a, Pablo P. Boix^{a,*}, Natalia Yantara^a, Mingjie Li^b, Tze Chien Sum^b, Nripan Mathews^{a,c}, and Subodh G. Mhaisalkar^{a,c,*}

Dr. Sjoerd A. Veldhuis, Dr. Pablo P. Boix, Dr. Natalia Yantara, Prof. Nripan Mathews, and Prof. Subodh G. Mhaisalkar

^aEnergy Research Institute at Nanyang Technological University (ERI@N), Research Techno Plaza, X-Frontier Block Level 5, 50 Nanyang Drive, Singapore 637553, Singapore

Dr. Mingjie Li and Prof. Tze Chien Sum

^bDivision of Physics and Applied Physics, School of Physical and Mathematical Sciences, Nanyang Technological University, 21 Nanyang Link, Singapore 637371, Singapore.

Prof. Nripan Mathews and Prof. Subodh G. Mhaisalkar

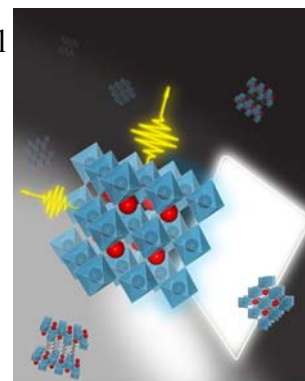
^cSchool of Materials Science and Engineering, Nanyang Technological University, 50 Nanyang Avenue, Singapore 639798, Singapore

Corresponding Author:

Dr. Pablo P. Boix (Email: PBPablo@ntu.edu.sg)

Prof. Subodh G. Mhaisalkar (Email: Subodh@ntu.edu.sg)

Keywords: Perovskite; light-emitting device; laser; electroluminescence; photoluminescence.



Abstract: Organic-inorganic hybrid perovskites have cemented their position as an exceptional class of optoelectronic materials thanks to record photovoltaic efficiencies of 21% as well as promising demonstrations of light-emitting diodes, lasers, and light emitting transistors. Perovskite materials with photoluminescence quantum yields close to 100%, perovskite light-emitting diodes with external quantum efficiencies of 8%, and current efficiencies of 43 Cd A⁻¹ have been achieved. Although perovskite light-emitting devices are yet to become industrially relevant, in merely two years these devices have achieved the brightness and efficiencies that organic light-emitting diodes accomplished in two decades. Further advances will rely decisively on the multitude of compositional, structural variants that enable the formation of lower-dimensionality layered and three-dimensional perovskites, nanostructures, charge transport materials, and device processing with architectural innovations. This article reviews the rapid advancements in perovskite light-emitting devices

and lasers. It addresses the key challenges in materials development, device fabrication, operational stability, and presents an outlook that will address market viability of perovskite light-emitting devices.

1. Introduction

The past three years have witnessed an unprecedented advance in the field of solar cells with perovskite metal halide, $\text{CH}_3\text{NH}_3\text{PbI}_3$, as the primary semiconductor of interest. The archetypical semiconductor forms nearly defect free, crystalline films that exhibit long-range charge transport, and efficient charge collection, yielding solar cells that rival the performance of industry standard silicon, with verified record efficiency of 21%.^[1] While much of the research community has been captivated by the potential to challenge silicon photovoltaics, perovskites have nevertheless, been making definitive strides as promising light-emitting materials with demonstrations of tunable amplified spontaneous emission and lasers,^[2, 3] light-emitting diodes in the infrared^[4] to bright green^[5] range, phosphor-like applications for yielding white-light emission, and balanced charge injection leading to radiative recombination within the channel of thin film transistors^[6] yielding red emission.

The detailed balance equation requires an external luminescence efficiency of close to 100% to attain the Shockley-Queisser limit of $\sim 33.5\%$ for solar cells; thus implying that an excellent solar cell material must also be an excellent light-emitter. As a result, perovskites have transitioned in a very short time from being a breakthrough material for solar cells to being regarded as an exceptional semiconductor material with wide-ranging applications in light emission.

Next generation light-emitting devices will be distinguished by their (i) high efficiency, high color quality, and tunability and (ii) low temperature solution-processing lowering both economic and energetic costs of manufacturing. These challenging objectives will require tuning of the emitter material, maximizing charge injection and light extraction efficiencies, minimizing non-radiative recombination related losses. Although inorganic LEDs have transformed artificial lighting and brought significant energy savings, these semiconductors rely on high-temperature, expensive vacuum based processing with epitaxial growth on expensive rigid substrates. The front-runners to replace these III-V semiconductors are

organic light-emitting diodes (OLEDs)^[7] and colloidal quantum-dot light emitting diodes (QLEDs).^[8] QLEDs are limited by a large non-radiative recombination from the high surface defect concentration; and although OLEDs have seen commercial applications, these are typically processed via vacuum-based sublimation, a method unsuitable for cost-effective large area processing. Conjugated polymers have been pursued for solution processability, however, the critical problem of forbidden (triplet exciton) radiative recombination fundamentally limits their intrinsic emission process. The problems faced by QLEDs and OLEDs would not be seen in perovskites because of the low defect densities^[2, 9, 10] and direct bandgap demonstrated. In particular, the intrinsic properties of organometallic halide perovskites, such as formation of nearly defect-free,^[11] crystalline films at low temperatures (~70-100 °C), high optical absorption / emission wavelength tunability, long-range ambipolar transport, efficient charge transfer, and injection to and from metallic contacts, are essential in its applicability to both solar cells and light-emitting devices. The electrical (e.g. diffusion length, mobility) and optical (e.g. photoluminescence quantum yield) qualities of metal halide perovskites, in the vicinity of the ones observed in inorganic semiconductors such as Si or GaAs, have manifested themselves in effective electroluminescence, optically pumped amplified spontaneous emission (ASE) and lasing. These applications require the generation of high amounts of localized charge carriers, so that the high extinction coefficient, low exciton binding energy and large diffusion lengths of solution-processed CH₃NH₃PbI₃ were assiduously leveraged.

The key parameter that serves as a figure of merit for high performance light-emitting materials is the photoluminescence quantum yield (PLQY) – defined as the ratio of emitted photons to those absorbed. On a LED level, the radiant efficiency (RE) or wall plug efficiency (WPE) is the electrical to optical energy conversion efficiency,^[12] and may be described as:

$$\text{RE (or WPE)} = \text{EQE} \cdot \text{LE} = \eta_{\text{injection}} \cdot \text{IQE} \cdot \eta_{\text{extraction}} \cdot (L / I \cdot V) \quad (\text{Eq. 1})$$

Here, the external quantum efficiency (EQE) is defined as the ratio of emitted photons to the number of electrons injected into the device, $\eta_{\text{injection}}$ is the proportion of electrons injected into the active emitter layer to the number of electrons passing through the device, internal quantum efficiency (IQE)^[13, 14] is the proportion of electron-hole recombinations that occur radiatively in the emitter layer, $\eta_{\text{extraction}}$ is the proportion generated photons in the emitter layer that exit the device, and luminous efficacy (LE) is the ratio of emitted (L) to injected energy ($I \cdot V$) by the source.

Amongst these multitude of metrics, the key figure of merits may include (i) EQE which measures how efficiently the device converts electrons to photons, and (ii) brightness (cd m^{-2}) (iii) current efficiency (CE; Cd A^{-1}). There is a correlation between efficient LED materials and suitable gain and laser materials. The light-emitting material used in an LED can, in principle, also be used as a gain medium in a laser if it is possible to achieve the transition from spontaneous emission to stimulated emission at higher input carrier densities. Indeed, the ultralow amplified spontaneous emission (ASE) thresholds of organometallic halide perovskites provide a strong impetus for light-emission applications using halide perovskites.

The extraordinary enhancement in the PLQY in the past two years (**Figure 1**) has now placed perovskites on par with the best-in-class solution-processed semiconductors, and it is an affirmation of the applicability of perovskites as light-emitting materials. Different approaches, such as synthesis of lower-dimensionality layered perovskites to increase the binding energies and oscillator strengths of the excitons, or increasing the spatial confinement, have been applied to maximize PLQYs (Figure 1). The high photoluminescence combined with the compositional flexibility of these materials place perovskites as robust technological candidates, distinguished by (i) high color purity (FWHM ~ 20 nm),^[15] irrespective of size of the crystallites due to the in-built quantum well structure in low-dimensionality perovskites^[16, 17] (ii) band-gap tunability to cover the entire spectrum of visible light and hence for

engineering white light emission in layered perovskites^[18, 19] (iii) low-to-moderate ionization energy (IE) to form stable functional interfaces.^[20]

In addition to possessing maximal external luminescence, a good light-emitting device requires efficient injection and transport of charge. An efficient injection process at the interfaces can reduce the energetic losses, whereas the use of energetically-matched contacts can minimize interfacial non-radiative recombination. In particular, balancing the electron and hole injection by tailoring the interfaces helps to focus the radiative recombination within the desired emitter material. In this aspect, metal halide perovskites meet the charge transport and charge injection requirements, with the high diffusion lengths and optimum interface formation with most of the employed contacts. In perovskite light emitting-diodes (PeLED), the emitter layer may comprise of 3D, layered, or nanostructured perovskites sandwiched between electron and hole transport layers and injecting contacts (**Figure 2a**). The performance of PeLEDs has rapidly progressed from under 1% to over 8% EQE in less than two years (**Table 1**); and CE, luminance are approaching the QDLED and OLED ranges (**Figure 3**). Although PeLEDs are yet to approach industrial applications, rapid improvements over the two-year period have been realized through leveraging OLEDs/QLEDs developments over the past decade. Further breakthroughs in PeLED performances are possible only by a combination of rational end-use designed materials, defect-free systems, and maximized external photoluminescence efficiencies. The material enhancement would include materials design and exciton engineering, optimized charge injection layers, and emission tunability to yield high color quality, purity, and white light emission (**Figure 4**).

Laser applications would also derive significant advantages from multi-dimensional and nanostructured perovskites (**Figure 2b**). In contrast to 3D perovskite thin films, nanoparticles and nanoplates form a natural resonant cavity to achieve population inversion required for amplified spontaneous emission (ASE) and lasing. The large degree of bandgap tunability reported for perovskite lasing, from near infra-red to ultraviolet, make this

technology suitable for a wide range of applications; and the optoelectrical properties have the potential to enable polariton, excitonic and free-carrier lasing. The current optically-pumped systems are an initial step towards a solution-processed electrically-pumped laser, a scientific and technologically challenging objective that perovskites must ultimately target.

In this review we will cover the evolution of perovskite materials and devices for light emission applications. We will disclose the physical and chemical characteristics which put perovskites in the spotlight, analyzing the rich diversity in composition and structure reported for this family of materials and their distinctive properties. This will include an analysis of the unique value offered by 3D and lower-dimensionality layered perovskites, as well as the detailed review of different morphologies and nanostructures, and the property tuning via control of its chemical composition. The application of these materials in functional devices will be analyzed in the subsequent section, presenting the state-of-art of PeLEDs and perovskite lasing, as well as device architecture innovations, loss mechanisms, and identifying limitations to be addressed in the photophysical properties. To conclude, we will discuss the challenges to be addressed, which include improving the device performance and size, finding replacement for Pb due to concerns over toxicity, developing of functional laser applications, and enhancing material and device stability.

2. Perovskite Materials for Light-emission

Perovskites, with general formula AMX_3 , are a well-known class of inorganic materials finding widespread deployment in ferro- and piezoelectric, magnetoresistive, semiconducting, catalysis applications. The rich diversity in properties is attainable owing to the multitude of large bivalent cations that may occupy the A-site (e.g. Ca^{2+} , Sr^{2+} , Ba^{2+} etc.), the smaller tetravalent cations (e.g. Ti^{4+} , Zr^{4+} etc.) at the M site, and oxygen occupying the X-site (**Figure 5a**). Organic-inorganic (hybrid) perovskites are different from their classical oxide counterparts with monovalent organic moieties introduced on the A-site, divalent metal cations at the M site, and typically halides at the X-site. The AMX_3 hybrid perovskite structure is formed by a three-dimensional (3D) network, with the organic A-site cations occupying the cavity between four adjacent corner-sharing MX_6 metal halide octahedra (e.g. $M = Pb^{2+}$, Sn^{2+} , Ge^{2+} , Cu^{2+} , Eu^{2+} , Co^{2+} , etc. and $X = Cl^-$, Br^- , I^- ,). The probability of forming (or not) the perovskite structure, can be estimated using the Goldschmidt tolerance factor (t) and the octahedral factor (μ).^[21-23] Here, t is based on the ionic radii (r) of the A, M, and X, constituents in $t = (r_A + r_X) / \sqrt{2} (r_M + r_X)$, and μ is defined as r_M / r_X . According to the tolerance factor, only the incorporation of small cations will result in perovskite formation ($t \approx 1$), although it is found empirically that for $0.80 < t < 0.90$ and $0.40 < \mu < 0.90$ cubic perovskites can form.^[22-25] This implies that the large ionic radii of Pb (1.19 Å) and the halides (e.g. iodide 2.20 Å), limit the ionic radius of the monovalent A cation to 2.9 Å; thus accommodating organic molecules consisting of less than two or three C-C or C-N bonds or inorganic cations such as Cs^+ (1.88 Å) are expected to fit in the 3D hybrid perovskite.^[24]

The first reports on light-emission^[26-28] and lasing^[29] from hybrid perovskites were already published in the 1990s. For example, large crystals of $(C_6H_5(CH_2)_2NH_3)_2PbI_4$ obtained via simple acid-base reactions, showed intense electroluminescence after applying a voltage of 24 V at liquid nitrogen temperatures.^[26] This layered perovskite material offers the possibility of enhanced structural stability from an inorganic backbone, while the optical

properties can be tuned by the organic cation. To overcome the low temperature limitation, a double-protonated 5,5'-bis(2-aminoethyl)-2,2':5',2'':5'',2'''-quaterthiophene (AEQT) dye was used as organic constituent in the hybrid structure, demonstrating room temperature electroluminescence.^[30] However, (AEQT)₂PbBr₄-based devices could only be fabricated via a thermal ablation method, since solution-processing was not possible due to the low solubility of the AEQT dye in common solvents and their incompatible wettability with the substrate. Since then, only few accounts on light emission from perovskites were reported, and the field seemed dormant for more than a decade. It was only in 2014, that room temperature light-emission from solution-processed CH₃NH₃PbX₃ perovskites was demonstrated.^[2, 5] Compared to expensive, vacuum-based processing of currently used solid-state light-emitting devices, the low-temperature processing conditions pose a very attractive alternative towards cost-effective large area optoelectronic applications. Following the breakthrough performance of perovskites in photovoltaic devices, CH₃NH₃PbI₃ and its anion substituted analogues were shown to display amplified spontaneous emission at thresholds as low as 12 μJ cm⁻².^[2, 31] In addition, it was also demonstrated that typical solar cell architectures (with mesoporous TiO₂ scaffold) also exhibit ASE at very low optical pump fluence thresholds (Figure 5b).^[2] First demonstration of light emitting diodes (LEDs) was also based on the halide substituted CH₃NH₃PbX₃ family (Figure 5c).^[5] By tuning the halide composition of the perovskite, the devices displayed bright green (517 nm) and red (630 nm) EL emission, with EQEs ranging 0.1-0.4%, respectively. Besides the devices based on the CH₃NH₃PbX₃ family, LEDs based on inorganic CsPbBr₃ were also recently reported.^[32] In addition to light-emission from thin emitter films, bright emission was also observed from nanostructured (nanoparticles, nanoplates, and nanowires) organic-inorganic and all-inorganic perovskites.^[15, 33-36] The propensity for tuning of the photophysical properties via cationic and anionic substitutions along with the additional range afforded by size and morphology manipulation amount to a broad palette of possibilities for light-emitting devices.

2.1 3D Perovskites and Lower-dimensionality Layered Perovskites

2.1.1. 3D Perovskites

The effective light-emission from organic-inorganic hybrid perovskites originate from their remarkable properties such as low defect densities, low non-radiative recombination, and high photoluminescence. The first demonstrated device achieved effective bimolecular recombination by spatial confinement of electrons and holes within the thin emitter layer (ca. 15 nm), thus overcoming the low exciton binding energy of the perovskite.^[5] The devices displayed bright green ($\text{CH}_3\text{NH}_3\text{PbBr}_3$; EL at 517 nm) and red ($\text{CH}_3\text{NH}_3\text{PbBr}_2\text{I}$; EL at 630 nm) EL emission, with EQEs ranging 0.1-0.4%, respectively, with a maximum brightness of 364 Cd m^{-2} for the green-emitting device. Commonly, the thin emitter films are prepared via spin-casting methods, in which dissolved precursors are spread on a substrate at high rotational speeds. For improved thin film morphology, one-step and sequential deposition techniques (adopted from photovoltaic devices) are often employed.^[37] For optimal light-emission from thin films, high surface coverage and smooth morphology are prerequisite, as non-radiative losses originating from shunt paths (e.g. due to incomplete surface coverage or pinholes) result in lower emission. By embedding the perovskite materials in a polymer matrix, pinhole-free films were obtained from poly(imide)^[38] or poly(ethyleneoxide)^[39] matrices and improved luminescence performance were displayed. Additionally, it has been suggested that the formation of metallic Pb (e.g. from incomplete perovskite formation at stoichiometric precursor ratios)^[40] may lead to non-radiative decay pathways originating from these defect trap states, thus posing a challenge to high luminescence efficiency in light-emitting devices. Addition of excess $\text{CH}_3\text{NH}_3\text{Br}$ during film deposition has been attributed to the suppression of Pb formation and improved efficiencies.^[40] It should be noted that this observation is in contrast with the need for excess lead reported for solar cell applications^[41] and further investigations in this direction would need to be pursued. Analogues of

$\text{CH}_3\text{NH}_3\text{PbX}_3$ are very moisture-sensitive and suffer from low thermal stability. Approaches taken in the photovoltaics research such as improved processability, efficiency, halide segregation, thermal and photo-stability with cation substitution or mixed cation perovskites (e.g. formamidinium (FA; $\text{HC}(\text{NH}_2)_2$),^[42, 43] and $[\text{HC}(\text{NH}_2)_2]_{0.83}\text{Cs}_{0.17}\text{Pb}(\text{I}_{0.6}\text{Br}_{0.4})_3$)^[44] would need to be explored for improved performance of these 3D thin film light emitters. Besides the methylammonium based perovskites, inorganic CsPbBr_3 perovskite thin film emitters have also yielded stable bright green emission (407 Cd m^{-2}) with narrow electroluminescence widths and low turn-on voltage.^[32] Improved performance was observed by modulating the precursor stoichiometry during thin film formation with an excess of CsBr ($\text{CsBr}:\text{PbBr}_2 = 2:1$) showing nearly 300% improvement in luminescence over the stoichiometric compositions. Besides the increased thermal stability compared to the $\text{CH}_3\text{NH}_3\text{PbX}_3$ family, bulk CsPbBr_3 exhibits other attractive features for light-emitting applications, such as long PL life-time ($\sim 2.5 \mu\text{s}$) and electron mobility ($\sim 10^3 \text{ cm}^2 \text{ V}^{-1} \text{ s}^{-1}$, comparable electron and hole mobility/life-time products,^[45] small exciton binding energy ($\sim 35 \text{ meV}$),^[46] and potentially better ambient stability.

2.1.2. Lower-dimensionality Layered Perovskites

In contrast to the 3D AMX_3 perovskites, layered perovskites of general formula $(\text{RNH}_3)_2\text{A}_{n-1}\text{M}_n\text{X}_{3n+1}$ ($n = 1$, pure 2D layered; $n = \infty$, 3D structure; and $n = \text{defined integer}$, quasi-2D layered structure) are formed when cations are introduced that do not fit in the cuboctahedral cavity between the MX_6 octahedra. The cubic symmetry is broken and the inorganic lead halide layers of the original 3D structure can be separated into $\langle 001 \rangle$ or $\langle 110 \rangle$ oriented slices or cuts to accommodate the larger cations (**Figure 6a**). Estimated on the ionic radii of typically used MX_6 constituents Pb^{2+} (1.19 \AA) and I^- (2.20 \AA), a layered perovskite structure, of general formula A_2MX_4 , forms when the ionic radius of the A-constituent exceeds approximately 2.6 \AA .^[24, 47] The inorganic layers are held together by weak van der Waals

forces and are fundamentally different from e.g. metal chalcogenide semiconductors, as here a rigid backbone is formed through covalent bonds between the metal cations and the Se or S atoms.^[48] In addition, these layered nanostructures can be considered as natural quantum well structures, where the inorganic layers act as ‘wells’ and the organic molecules as ‘barriers’ (see Figure 6b).^[17] They possess very large binding energies (several hundreds of meV) due to enhanced electron-hole interactions originating from the very different dielectric constants of the ‘well’ and ‘barrier’,^[49] while the decreased symmetry diminishes the forbidden electronic transitions and contributes to the enhancement of the photoluminescence intensity or quantum yield. As a result of the strong confinement in two dimensions and wide compositional flexibility, these layered perovskites are ideal for light-emitting applications.^[18, 19, 50] Moreover, the binding energy is directly tuned by the number of inorganic layers n in the structure, where $n = 1$ and $n = \infty$ represent the ‘pure’ layered vs the 3D perovskite, respectively (Figure 6a). Higher-order layered compounds ($A'_2A_{n-1}M_nX_{3n+2}$) with $n = 2, 3, 4$, etc. are formed through intercalation of a mixture of cations, capable of forming both the 3D (A' ; e.g. CH_3NH_3^+ , $\text{HN}=\text{CHNH}_3^+$, or Cs^+) and layered perovskite structure (A). These compounds can be considered multi-dimensional, as their dimension lies somewhere between layered 2D and 3D. Although charge transport between the inorganic layers is limited due to the large spacing between the individual layers, vertical crystal growth (*i.e.* inorganic sheets perpendicular to the substrate surface) techniques could help overcome this limitation.^[17, 51]

The increased structural freedom creates new possibilities to incorporate larger and more complex structures with tailored photophysical and electronic transport properties beyond the archetypal perovskite structure such as conjugated systems with π - π interactions (e.g. phenylethylamines^[49]), organic dyes (e.g. thiophenes^[52]), or fluorophores. However, the nature of intercalated molecules has implications with respect to the layered structure. For example, hydrogen bonding between the amine and bridging/terminal halides strongly influence the orientation and conformation in which the layered perovskites are formed.^[24] It

has been shown with van der Waals-corrected DFT calculations; that the orientation of the organic molecules play a fundamental role in determining the electronic properties of the layered material.^[53] The impact of intercalating various types of organic molecules on the structure and properties of the layered perovskite are discussed below.

2.1.2.1. Aliphatic, Bi-functionalized and Cyclic Amines

Aliphatic amines are structurally the simplest organic cations to form a layered perovskites (*i.e.* $(C_mH_{2m+1}NH_3)_2PbX_4$). The interlayer spacing is directly tuned by the chain length of the amine, and increases monotonically from approximately 4 to 14 Å for $m = 4-12$, respectively. Despite the increasing interlayer distance, the size of the quantum well remained unchanged, and exciton binding energies of ca. 320-420 meV were measured.^[54, 55] One of the earlier reports on multi-dimensionality shows that often thickness-dependent absorption and emission footprints are visible during optical characterization.^[56] For example, methylammonium lead iodide ($n = \infty$) has an optical band edge and PL emission around 753 nm. However, introduction of different amounts of decylammonium resulted in the formation of lower-dimensional layered perovskites ($n = 1, 2, 3$ to ∞ , respectively). Due to strong confinement in the ‘pure’ layered structure ($n = 1$), sharp excitonic absorption bands were observed at much smaller wavelengths than the luminescence band. Higher-order perovskites, on the other hand, displayed multiple absorption maxima at higher wavelengths related to their inorganic layer thickness.^[56] Similar footprints were observed in PL spectra layered structures of $CH_3NH_3PbBr_3$ in presence of octylammonium ligands.^[57] Nanoplates of $n = 2$ exhibited quantum confinement, and excitonic absorption blue-shifted approximately 0.5 eV blue-shifted compared to the bulk 3D crystal. Besides changes in the optical properties, changes in electronic properties have also been observed, e.g. the increase in perovskite layers n in $(C_4H_9NH_3)_2(CH_3NH_3)_{n-1}SnI_{3n+1}$ displayed a transition between semiconducting and metallic behavior.^[58]

Although many of these layered and multi-dimensional perovskites are formed via acid-base reactions,^[59] or slow precipitation from solution-phase,^[18, 19, 51, 60] a different approach has been reported recently.^[61] Multi-dimensional perovskites were formed by dipping a thin film of ‘pure’ 2D ($n = 1$) perovskite $(\text{IC}_2\text{H}_4\text{NH}_3)_2\text{PbI}_4$ in a $\text{CH}_3\text{NH}_3\text{PbI}_3$ ($n = \infty$) solution in 2-propanol/toluene (Figure 6e). By controlling the dipping time, the dimensionality was tuned between a layered lower-dimensional and bulk 3D perovskite structure, resulting in reduced optical band gaps (2.02 to 1.62 eV at 0 and 5 min, respectively). At longer dipping times, the absorption bands associated with layered perovskites became less noticeable, indicating an increased stacking of the lead halides lattices. Within 5 min, PL emission similar to $\text{CH}_3\text{NH}_3\text{PbI}_3$ was observed, implying near complete formation of the 3D structure.

Recently, it was demonstrated that layered PbBr_2 perovskites crystals of N^1 -methylethane-1,2-diammonium (N -MEDA)[PbBr_4] and N^1 -methylpropane-1,3-diammonium (N -MPDA)[PbBr_4] formed $\langle 110 \rangle$ and $\langle 001 \rangle$ oriented structures (Figure 6c-d).^[18] Despite the difference of only one carbon in chain length for N -MEDA and N -MPDA and the similarity between the two absorbance spectra, completely different photoluminescence is observed; the $\langle 001 \rangle$ sheets display sharp blue emission at approximately 420 nm, whereas the $\langle 110 \rangle$ sheets show broad white-light emission (maximum at 558 nm; PLQY $\sim 0.5\%$) covering the whole visible spectrum. Crystals with the N -MEDA ligands replaced by EDBE, (ethylenedioxy)-bis-(ethylammonium), yielded ‘warm’ and ‘cold’ white-light emitting crystals (color rendering index > 84) with quantum efficiencies of 2 and 9 % for the corresponding Cl and Br lead perovskites, respectively.^[19] These single-source emitters can potentially replace the use of phosphors in the current white-light LEDs. The phosphors often suffer from high efficiency losses due to e.g. self-absorption at specific wavelengths as well as changes in the emissive color caused by different degradation rates of the individual phosphors. Contrary, single-source (N -EDBE)[PbBr_4] showed great structural stability, and the color emission and

intensity remained unchanged after continuous illumination of more than three months (4 W lamp at 365 nm).^[19] Cyclohexylamine-based $(\text{C}_6\text{H}_{11}\text{NH}_3)_2\text{PbBr}_4$ layered perovskites also display broad white-light emission, albeit it at 90 K, with a PL maximum 2 eV and FWHM of ca. 660 meV.^[50]

2.1.2.2. Conjugated Systems and Chromophores

Beyond simple amines, layered perovskites have also been formed by larger and more complex molecules, such as conjugated molecules and chromophores. The π - π interactions within and between the molecules strongly influence the ordering (conformation and orientation) between the inorganic layers. For example, well-ordered inorganic CuX_6 octahedral layers are formed in $(\text{C}_6\text{H}_5(\text{CH}_2)_2\text{NH}_3)_2\text{CuX}_4$ ($\text{X} = \text{Br}^-$ or Cl^-) in which the ammonium groups are hydrogen bonded to the halides, while distorted layered structures were formed with PbCl_6 based perovskites^[24, 52]. In addition, the optical performance is strongly dependent on the chain length of the R-group in R-NH_3^+ .^[62, 63] A five-fold PL increase was observed in $(\text{C}_6\text{H}_5(\text{CH}_2)_m)_2\text{PbBr}_4$ by changing m from 1 to 2. A further increase to $m = 3$ resulted in only ~22% of original value of $m = 1$. In one of the early reports, large single-crystalline $(\text{PEA})_2\text{PbI}_4$ crystal grown from solution displayed green EL emission at low temperatures. Via a spray-casting method, 50-500 nm-sized layered crystals were formed exhibiting green emission at similar wavelengths as single crystals.^[64] Although the particle size was much larger than the exciton Bohr radius, quantum confinement originating from the layered structure was observed (interlayer spacing ca. 1.6 nm). As opposed to large layered structures formed via self-organization, film deposition from solution is more amendable, while the stability of the layered perovskite is retained.

The accommodation of double-protonated 5,5''-bis(2-aminoethyl)-2,2':5',2'':5'',2'''-quaterthiophene (AEQT) chromophore in between PbBr_4^{2-} sheets, results in a $\langle 001 \rangle$ oriented structures that exhibits green photoluminescence. Unlike the straight configuration of the

organic molecules in $\text{C}_6\text{H}_5(\text{CH}_2)_2\text{NH}_3)_2\text{CuX}_4$, the dye molecules are arranged in a herringbone-type configuration, where the amines are hydrogen-bonded to both bridging and terminal halides.^[52] Devices from thick layered perovskites (300 nm) displayed bright green emission with a maximum efficiency of 0.1 lm W^{-1} (at 8V).^[30] Oriented layered films using other chromophores such as naphthalene and azobenzene were also reported.^[65] These are interesting materials, as the excited states of the chromophores are higher in energy than the inorganic layers and thus the emission originates from the inorganic backbone.

2.2. Nanostructured Perovskites

One of the major advantages over traditional inorganic oxides is the low energy barrier to form organic-inorganic hybrid perovskites; where a crystalline phase is readily obtained by merely mixing and grinding the precursor salts at room temperature. Although this method suffers from lack of precise experimental control, it exemplifies the ease with which the organic cations can diffuse into the inorganic framework. Typically, perovskite synthesis is performed via wet-chemistry routes, allowing for mixing at a molecular level, and resulting in high phase purity materials. By carefully controlling the reaction conditions (e.g. temperature, solvent, ligands), hybrid perovskites of various morphologies (0D quantum dots to 3D single crystals) and sizes (stretching 6 orders of magnitude) can be prepared (**Figure 7**). Nanostructuring can be achieved in both layered as well as 3D perovskites. For example, $5 \times 5 \times 2 \text{ mm}^3$ -sized $\text{CH}_3\text{NH}_3\text{PbBr}_3$ single-crystals (bulk) are formed within several hours by exploiting its lower solubility in solvents at elevated temperatures,^[66] and $\text{CH}_3\text{NH}_3\text{PbBr}_3$ nanoparticles (NPs),^[34, 67-69] layered sheets,^[36, 57] and nanowire (NWs)^[70, 71] were also formed (Figure 7b-e).

These examples only briefly showcase the ease in which a wide variety of nanostructured perovskites can be obtained. In recent years, nanostructuring of materials has become increasingly important, as certain phenomena (absent in bulk materials) are only

observed at the nanoscale. The material's properties are directly tuned during synthesis and are closely related to their size (and size distribution). For example, judicious control over synthesis conditions (e.g. precursor concentration, reaction temperature, choice of ligands, etc.) may result in different optical properties originating from e.g. quantum size effects^[16] or anisotropic particle growth.^[72] The typical synthetic strategies towards organic-inorganic hybrid perovskites, and the effect on the material's photophysical and morphological properties, will be discussed below (color-tunability is discussed in a subsequent section).

2.2.1. Nanoparticles (NPs) and quantum dots (QDs)

Currently, most of the reported synthetic routes leading to the formation of hybrid perovskite nanoparticles (NPs), can be divided into two distinct strategies. $\text{CH}_3\text{NH}_3\text{PbX}_3$ NPs are predominantly formed using the ligand-assisted reprecipitation method (LARP). Polar solvents, capable of dissolving the inorganic lead and ammonium halide (MA-X) salts, are injected into a nonpolar 'poor' solvent in the presence of coordinating ligands to stabilize the newly-formed particles. Due to the temperature instability, these syntheses are conducted at low temperatures ($<80^\circ\text{C}$).^[16, 34, 67-69, 73, 74] Alternatively, replacement of the CH_3NH_3^+ cation with Cs^+ yields inorganic perovskites with increased structural stability. These inorganic CsPbX_3 NPs are prepared using a hot-injection method at temperatures in excess of 150°C . The NPs are typically formed by swiftly injecting Cs-oleate, formed through reaction between Cs_2CO_3 and oleic acid (OA), in a solution of PbX_2 ($\text{X} = \text{Cl}^-, \text{Br}^-, \text{or } \text{I}^-$) in non-coordinating solvents (such as 1-octadecene; ODE) at temperatures ranging $140\text{-}200^\circ\text{C}$ under N_2 atmosphere^[15, 75-77] Here, the presence of OA and oleylamine (OAm) ligands help to inhibit the crystal growth, passivated the surface defects, and contribute to colloidal stability. This method has been successfully employed in the fabrication of high quality inorganic semiconductor NPs.^[78] One of the remarkable features of the hybrid perovskites is that, as

opposed to semiconductor QDs, no additional surface passivation is necessary to achieve high PLQY, and dangling bonds (from surface ligands) did not play a role in the PL emission.^[15, 76]

Colloidal $\text{CH}_3\text{NH}_3\text{PbBr}_3$ cubic nanoparticles (~ 6 nm) using the LARP method (Figure 7b)^[34] were precipitated (at 80 °C) in the presence of long-chained ammonium bromide ligands, and exhibited bright green PL emission at 527 nm, with a PLQY of approximately 20%. Increased reaction temperatures (120 °C), yielded equal quantum efficiencies and PL emission wavelengths,^[79] showcasing the rigidity and high reproducibility of the method. The synthesis was further optimized by increasing the organic/inorganic precursor ratios and narrow PL emission (FWHM ca. 30 nm, at 520 nm), and significantly improved PLQY values of 83% were recorded.^[67] The improvement stems mainly from better surface passivation by the ligands. Quantization effects were observed for 1.8-3.6 nm-sized $\text{CH}_3\text{NH}_3\text{PbBr}_3$ NPs prepared at 0-60 °C, respectively; accompanied with blue-shifted PL emission at 475, 500, and 520 nm.^[68] Especially at low temperatures, ligands will most likely stay on the surface of the NPs, strongly affecting their growth.^[80] Although the highest PLQY to date (93%) was recorded, the effect may also be attributable to size-exclusion from very high centrifugation speeds (14500 rpm) used. In addition, only the supernatant phase (containing only the smallest NPs) was used, instead of the precipitate.^[34, 67] Nanoparticles of $\text{CH}_3\text{NH}_3\text{PbBr}_3$ (~ 3.3 nm) have also been reported utilizing *n*-octylamine (OLA) as the surface capping ligand, with the supernatant colloidal solution exhibiting high PLQY (~ 50 -70%).^[69] A small degree of quantum confinement was suggested with a blue-shifted PL emission at ca. 515 nm. The PL life times of these NPs (~ 6 -24 ns)^[68, 69] are significantly lower than in bulk $\text{CH}_3\text{NH}_3\text{PbBr}_3$ (~ 100 ns),^[81] indicating that PL decay is predominantly originating from radiative exciton recombination.

Despite the high quantum yields and colloidal stability of methylammonium halide NPs (>5 months; in air under dark conditions^[67]), a major shortcoming arises from its instability in polar solvents (also used to dissolve the precursors prior to NP formation). To

overcome this, Vybronyi *et al.* synthesized $\text{CH}_3\text{NH}_3\text{PbX}_3$ without the use of polar solvents.^[82] Although the precipitate displayed lower quantum efficiencies (25-50%) than previously reported for $\text{CH}_3\text{NH}_3\text{PbBr}_3$ NPs, it shows that an alternative synthesis route without the use of polar solvents is possible. Other approaches involved the formation of $\text{PbS}/\text{CH}_3\text{NH}_3\text{PbX}_3$ core-shell NPs via ligand-exchange reactions, in which the halide successfully passivated the surface traps on the PbS nanoparticle surface.^[83, 84] Light-emission associated with charge transfer between PbS/CdS NPs and $\text{CH}_3\text{NH}_3\text{PbI}_{3-x}\text{Cl}_x$ has also been reported.^[85]

Beyond the methylammonium perovskite family of materials, color-tunable CsPbX_3 perovskite NPs (4-15 nm diameter) using the hot-injection method at temperatures ranging 140-200 °C (**Figure 8a**) have also been reported.^[15] The resulting NPs exhibited very high quantum yields of 50-90 % and narrow emission line widths of 12-42 nm. Owing to the large Bohr radius calculated for CsPbCl_3 (5 nm), CsPbBr_3 (7 nm), and CsPbI_3 (12 nm), quantum confinement was observed.^[15] With transient absorption spectroscopy (TA) it was determined that the high quantum yields arise from negligible electron-hole trapping pathways,^[86] and an average PL life-time of $\tau = 1\text{-}29$ ns was recorded, with the lowest value for CsPbCl_3 (~ 1 ns; PLQY $\sim 50\%$).^[15, 77, 86] Unlike semiconductor QDs, no spectral broadening originating from high surface trap densities (due to the large surface-to-volume ratio), or size-distribution, were observed.^[77] In addition, CsPbX_3 does not show changes in optical bandgap at elevated temperatures, which is important for color quality retention in light-emitting devices (*i.e.* heating effects).^[77]

2.2.2. Nanoplates (NPLs)

Currently, NPLs have not been extensively used in optoelectronic devices, and only one report on their use in light-emitting devices^[87] is published. However, significant efforts have been made to synthesize these nano-sized materials for increased photoluminescence quantum yield and structural stability. Besides the use of long-chained ligands to form lower-

dimensionality layered perovskites along (100) slices and (110) cuts of the 3D structure, they can also be used to selectively inhibit the crystal growth direction in one dimension. Thin quasi-two-dimensional perovskites are then formed by morphological control, rather than by separation of the individual inorganic layers.^[87]

Formation of 1.2 nm thick $\text{CH}_3\text{NH}_3\text{PbBr}_3$ NPLs was demonstrated via non-templated routes and,^[57] although PL emission could not be observed due to the low NPLs concentration, the absorption peak at 431 nm was ca. 0.5 eV blue-shifted compared to that in the bulk.^[56, 88] Additional absorption maxima at 431, 451, 472, and 525 nm, corresponding to $n = 1, 3, 4$, and ∞ , respectively, were in agreement with earlier reports for layered perovskites.^[56, 59] Similarly, changes in the size, morphology, and PL emission were observed by adjusting the ratio between methylammonium and octylammonium cations^[16, 73] The blue-shifts originating from quantum confinement, are partially counteracted due to the high binding energy (several hundred meV) found for NPLs of $n < 3$.^[16] The calculated excitonic Bohr radius of 1.36 nm is in agreement with the estimation of Tyagi *et al.* (1.4-2 nm) and corresponds to a platelet thickness between $n = 2$ -3.^[16, 57] This corroborates with earlier finding, where confinement for $n = 2$ structures was observed.^[56]

Tuning of the morphology of $\text{CH}_3\text{NH}_3\text{PbX}_3$ ($\text{X} = \text{Br}^-$ or I^-) NPs from nanocubes to NPLs and NWs, was achieved by adjusting the ratio between the OAm and OA ligands.^[82] The $\text{CH}_3\text{NH}_3\text{PbBr}_3$ nanoplates exhibited blue PL emission and absorption at 465 and 450 nm, respectively, with a PLQY of ~18%. Self-organization of these platelets led to the formation of wire-like structures, with green PL emission at 530 nm (PLQY ~15%). Similar asymmetric growth and self-assembly in hierarchical structures was observed by controlling the reaction temperature of the CsPbBr_3 NC synthesis.^[15] Instead of green-emitting nanocubes (8-10 nm; formed >150 °C), reactions at 130 and 90 °C yielded cyan and blue-emitting NPLs, respectively. The remarkably high quantum yields (up to 84%) indicate a low concentration of surface defects.^[89]

Beyond NPLs of 3D materials (e.g. $\text{CH}_3\text{NH}_3\text{PbBr}_3$, CsPbBr_3) atomically thin, uniformly square-sized sheets of layered perovskite $(\text{CH}_3(\text{CH}_2)_n\text{NH}_3)_2\text{PbBr}_4$ ($n = 3$ and 7) have also been prepared.^[16, 48] A ternary solvent was employed to facilitate controlled precipitation of NPLs and utilizing the different precursor solubility in each solvent.^[48] The thinnest sheets (~ 1.6 nm) showed deep blue PL emission at 406 nm and PLQY of $\sim 26\%$, compared with $<1\%$ in the bulk crystal, was attributed to quantum confinement effects.^[48] For layered $(\text{CH}_3(\text{CH}_2)_7\text{NH}_3)_2\text{PbBr}_4$, slightly red-shifted PL emission (at 427 nm) was observed which can be explained by reduced confinement from larger effective spacing between the inorganic layers.^[16] Although ligands can effectively help ‘steer’ the reaction and morphology of the perovskites, post-processing and purification steps are necessary for thin film formation. To overcome this problem, Yuan *et al.* described a one-pot synthesis approach using a mixture of PbBr_2 , HBr , OLA and benzyl amine in DMF, which circumvented the pre-preparation of ammonium salts and ligands.^[90] The formed NPLs, with thicknesses and lengths of 100-150 nm and 1-4 μm , respectively, showed narrow PL emission ranging 403-413 nm, with a PLQY of $\sim 53\%$. Quantum yields as high as 85% were obtained when smaller methyl amine was used, instead of benzyl amine.^[87] In addition, the non-radiative decay was lower the radiative decay (PL life-time 3.1-4.7 ns; approximately two times faster than NPs), indicating minimal surface and self-quenching effects.^[90]

The general strategy in the abovementioned methods is based on the direct formation of the nanoplates. The precursors are pre-mixed in a ‘good’ solvent, and NPLs are subsequently precipitated from solution. However, the transformation via an intermediate phase has also proven very successful. Not only can the hybrid perovskite phase form, the pre-existing morphology of the seed can also be retained. Hassan *et al.* demonstrated this concept and synthesized highly luminescent 5.5 nm-sized $\text{CH}_3\text{NH}_3\text{PbX}_3$ layered halide perovskites (PLQY $\sim 20\%$) from seeded PbX_2 NPs ($\text{X} = \text{Br}^-$ or I^-), see Figure 7c.^[33] The PL emission at 505, 565, and 600 nm was tuned by controlling the thickness of the layers to $n = 1$,

2, and 3 using long-chained ligands. Quantization due to spatial confinement was observed, despite larger NPs sizes than the reported Bohr radius,^[16, 57] Similarly, Zhang *et al.* formed $\text{CH}_3\text{NH}_3\text{PbX}_3$ NPLs from pre-formed PbX_2 ($\text{X} = \text{Cl}^-$, Br^- , or I^-) platelets using vapor-phase deposition (Figure 7d).^[36] Lead halide platelets were converted to the corresponding $\text{CH}_3\text{NH}_3\text{PbX}_3$ phase by evaporation of a MA-X source, while maintaining the hexagonal lead halide geometry. Despite a PLQY $\sim 17\%$, the high binding energy (45 ± 11 meV), long-diffusion lengths, and PL life-time of ~ 2.6 ns demonstrate that NPLs have favorable properties for efficient light-emission.

2.2.3. Nanowires (NWs) and nanorods (NRs)

One-dimensional structures have attracted considerable attention due to their high surface-to-volume ratio and structural anisotropy. For this reason, they are often employed in sensing and catalysis applications. To date, only a few reports have been published on the preparation of halide perovskite NWs for LED,^[35, 70] lasing,^[3, 71] and photodetector^[91] applications. For example, photoluminescent $\text{CH}_3\text{NH}_3\text{PbX}_3$ and CsPbX_3 ($\text{X} = \text{Cl}^-$, Br^- , or I^-) NWs has been demonstrated.^[35, 70, 71] The $\text{CH}_3\text{NH}_3\text{PbBr}_3$ NRs were grown directly on PEDOT:PSS coated ITO/glass substrate by converting lead acetate NWs via immersion in a $\text{CH}_3\text{NH}_3\text{Br}$ solution.^[70] Green PL and EL emission (at ca. 533 nm), was demonstrated from a light-emitting array of NWs, indicating good electron and hole-injection. Single-crystalline CsPbX_3 NWs (12 nm width and lengths up to 5 μm ; Figure 7e) formed sequentially through assembly of nanocubes at prolonged reaction times using the method described by Protesescu *et al.*^[15, 35] A similar type of self-organization of $\text{CH}_3\text{NH}_3\text{PbX}_3$ ($\text{X} = \text{Br}^-$ or I^-) and CsPbBr_3 of nanoplates into larger wire-like structures was observed.^[82, 89] The CsPbBr_3 NWs showed a small degree of confinement, as a 60 meV blue-shift was observed in the PL spectra.

2.4. Color Tunability

Halide perovskites enjoy great structural flexibility, and their morphology can be conveniently manipulated during synthesis, resulting in a wide variety of shapes and sizes. The band gap in these perovskites can be tuned by e.g. (partial) substitution of the cation, or by changing the halide source during synthesis. This strategy has already been exploited in photovoltaic devices, and mixed-cation and mixed-halide perovskites have already been synthesized for better stability and optimal band gap.^[44] Although for single-junction solar cell applications a small band gap material is required for high efficiency, this is not a prerequisite for light-emitting devices or good light emission in general. Instead, materials with PL emission across the visible spectrum with narrow emission line-widths and limited spectral overlap are required.

2.4.1. Anion-based Color-tuning

Hybrid perovskites have already demonstrated that variation of the anion in e.g. $\text{CH}_3\text{NH}_3\text{X}_3$ (Cl^- , Br^- , or I^-), tunes the bandgap from 3.11 eV, to 2.3 eV, and 1.55 eV, respectively.^[92] Color-tuning by partial halide substitution during the perovskite synthesis proved successful, irrespective of the reaction conditions (e.g. temperature), reaction media (*i.e.* solution and thin films), cationic nature (*i.e.* $\text{CH}_3\text{NH}_3\text{PbX}_3$ or CsPbX_3), or sample morphology (e.g. NPs, nanoplates, or NWs). For example, the PL emission of CsPbX_3 NPs could be tuned across the whole visible spectrum (Figure 8a-b). The use of different halide sources yielded NPs of high quantum yield and high color-purity with narrow PL emission at approximately 410 nm ($\text{X} = \text{Cl}^-$), 525 nm ($\text{X} = \text{Br}^-$), and 700 nm ($\text{X} = \text{I}^-$), covering a wide color gamut.^[15] The use of different halide stoichiometry yields PL emission exactly in between the expected values for the ‘pure’ perovskite NPs (see Figure 8a-b).

This color-tuning approach was extended by exploiting the ionic nature of the hybrid perovskites, in particular the high mobility of halides. Anions could be replaced in-situ by subjecting pre-formed NPs (or thin films) to anion-exchange reactions.^[75, 76, 93] For example,

anion-exchange was initiated by swiftly injecting a different halide precursor to purified CsPbBr₃ NPs in toluene at temperatures <40 °C. In most cases, the anion exchange proceeds rapidly, and is finished within seconds. Throughout the exchange reaction, a gradual shift in PL emission can be observed (Figure 8c). The figure shows time-resolved PL emission and intensity during the exchange reaction from CsPbBr₃ to CsPbI₃, in which an excess of oleylammonium iodide (3:1) is added to CsPbBr₃ NPs. Immediately after injection, the PL emission shifted to higher wavelengths due to the formation of iodide-rich domains. This rapid color change was also observed in the transformation of thin film CH₃NH₃PbBr₃ to CH₃NH₃PbI₃, although prolonged reaction times were necessary to form a homogeneous solid solution.^[93, 94] By carefully adjusting the ratios of the incoming and parent halide, the PL emission was tuned across the whole visible range (ca. 410-690 nm).^[75, 76] Exchange reactions were possible between all halide combinations, except Cl⁻ and I⁻, due to the large difference in ionic radii (1.81 Å and 2.20 Å, respectively) and lattice mismatch of the parent perovskites phases. From X-ray diffraction (XRD) and microscopy studies, it was also observed that not only the morphology of the parent perovskite NPs remains unchanged after anion exchange, the initial crystal structure is also retained.^[75, 76] Cubic CsPbI₃ NPs were prepared from cubic CsPbBr₃ through anion exchange, resulting in highly luminescent NPs, whereas direct synthesis yields the non-luminescent orthorhombic phase.^[76] Although a cubic-to-tetragonal phase transition was observed for iodide-exchanged CH₃NH₃PbBr₃ NPLs due to the larger ionic radius of iodide compared to bromide, the morphology was unaffected.^[93] Contrary, both single-crystalline tetragonal structure and morphology of CH₃NH₃PbBr₃ NWs was retained after vapor-phase halide exchange with CH₃NH₃I at 150 °C.^[70] The concept of facile exchange reactions has been further demonstrated through the cross-exchange of halides from discrete NPs (see Figure 8d).^[75, 76] Simply mixing e.g. the pure CsPbBr₃ and CsPbI₃ NPs initiates the exchange reactions, and instantaneous red and blue shifts are observed in the PL spectra, respectively. Full exchange occurs within 20 min, and a single PL peak indicates that

the halides are homogeneously distributed within NPs (*i.e.* CsPbBr_{1.5}I_{1.5}; Figure 8d panel 2),^[75] and the PLQY, PL emission, and PL line widths are equivalent to those obtained from direct synthesis or direct halide exchange.^[76]

Although the ease with which halides exchange take place can be exploited to tune the emissive colors of NPs or thin films, it poses severe problems when films of different halide composition are stacked. Halide ‘leeching’ was observed when Br⁻ (green emission) and I⁻ (red emission) containing films were deposited sequentially, with subsequent loss of the individual PL emission.^[73] Anion-exchange was inhibited by embedding the NPs in a polymer matrix, and no significant shift in PL emission was observed for both films. By employing this strategy, green and red emitting films were deposited on a blue-emitting GaN chip, and white-light emission from perovskite NC films was demonstrated.^[73]

2.4.2 Cation-based Color-tuning

The halide exchange reactions enable tunability of the PL emission to any desired wavelength across the visible spectrum. Cation substitution can also be employed to tune the wavelength of nanostructured perovskites,^[16, 73, 95] although usually on a much smaller wavelength range. Cation substitution is used as a common strategy to change the color emission, e.g. Ag₂Se NPs and PbS NRs from CdSe NPs and CdS NRs, respectively.^[96, 97] Similar to the halide exchange in perovskites,^[75, 76] the pre-existing morphology can be preserved after cation substitution. Cation substitution of CsPbBr₃ NPs with CH₃NH₃⁺ cations from methylammonium bromide (MA-Br),^[75] resulted in a PL shift from 510.2 to 525.4 nm, similar to the PL value (527 nm) observed for CH₃NH₃PbBr₃.^[34] A slight lattice expansion observed in the XRD patterns would further support the replacement of Cs⁺ with the larger CH₃NH₃⁺ cations.^[75] Although octylammonium bromide (OA-Br) has significantly improved the PLQY of CH₃NH₃PbBr₃ NPs by effectively passivating the surface and inhibiting crystal growth,^[67] increased concentrations result in blue-shifts in the PL emission due to the concurrent

formation of lower-dimensional layered perovskites (Figure 8e).^[16, 73] At low MA-Br:OA-Br ratios (<40% OA-Br) the PL emission remains virtually unchanged (517-519 nm), however, rapid blue-shifts are observed at higher ratios. At ratios <40%, OA-Br still acts as a capping ligands, restricting the growth of the formed NPs. This is supported by TEM microscopy observations, as predominantly small crystals are formed.^[16, 73] At ratios >60% OA-Br, multiple maxima originating from both mixed (MA/OA)PbBr₃ NPs and layered (OA)₂PbBr₄ perovskites are observed in the absorption spectra,^[73] and lower quantum yield are recorded.

2.5. Integration of Perovskite Emitters into Light-emitting Devices

Although halide perovskites exhibit remarkable optoelectronic properties, their integration into functional light-emitting devices requires further consideration. The combination of strong photoluminescence (up to 70% at high photon fluxes)^[31] and good electroluminescence properties in solar cell device configuration^[4, 98] has projected the organic-inorganic halide perovskite material as a perfect candidate for PeLEDs. Besides the emitter materials, the choice of matching electron and hole transporting materials and their integration into a light-emitting device are critical to define the device characteristics. To minimize energetic mismatch and minimize non-radiative recombination, multi-layered device structures and optimization of a plurality of interfaces would be essential to leverage the material's full potential.

Due to the attractive merits such as large absorption coefficients, ultralow bulk defect densities, slow Auger recombination and long range carrier diffusion length, the hybrid perovskite materials are also considered as a new class of optical gain media for the lasing applications. The easy solution processability at the low-temperature allow this kind of materials can be embedded into a wide range of cavity resonators which are attractive for the realization of on-chip coherent light sources. However, despite the success in achieving optically pumped hybrid perovskites lasers with relatively low pump fluence threshold,

electrically-driven laser remains a significant challenge and has not been realized yet. Many challenges, such as to fulfil requirements of the higher injection current densities, lower carrier threshold, and lower heating effects, need to be overcome in the future.

3. Light-emitting Devices

This section addresses the use of perovskite for lighting applications. As the main device concept, PeLEDs rely on electrical charge injection, transport, and radiative recombination. The role of the various device components, as well as the different reported device architectures will be discussed in this section. Other device configurations based on perovskites, such as light-emitting transistors and light-emitting electrochemical cells based on perovskites are also considered. In the last subsection, the working mechanisms and performance losses will be analyzed.

3.1 Perovskite Light-emitting Diodes (PeLEDs)

In general, the PeLED device architectures consist of front transparent electrode (e.g. FTO, ITO), electron transporting material (ETL; e.g. TiO₂, ZnO, F8, TPBi, BCP, etc.), emitter, hole transporting material (HTL; e.g. PEDOT:PSS, TFB, spiro-MeOTAD, Poly-TPD, etc.), and back electrode (**Figure 9**). The PeLED architecture may be generalized as ETL/perovskite/HTL and HTL/perovskite/ETL configurations; with the generated light transmitting through the ETL and transparent electrode for the former and through the HTL for the latter (**Figure 10b-c**). Ideally, the carriers that are injected through the electrode should be transported efficiently to the emitter, confined to promote radiative recombination (*i.e.* electroluminescence). Losses may include both electrical and optical and in addition to the emitter material, design, and selection of the interfaces is critical for high performance devices. Detailed device considerations including emitter materials processing, selection and

integration of ETL and HTL, working mechanisms of LEDs, and finally losses are discussed in detail in subsequent sections.

3.1.1. Tailoring the Band Alignment of the Interfacial Layer (i.e. HTL and ETL)

A device is only as efficient as the interfaces that inject the charges and the multi-layered structures that facilitate out-coupling of light. In this context, it is the interface that defines the device; and in particular, the choice of appropriate ETL and HTL are of critical importance to the device efficiencies. The selection of ETL and HTL is governed by the energy band alignment (to inject the carrier in the emitter) and by the materials' chemical compatibility (this includes considerations on the solvents, in the case of solution processed devices). Naturally, HTL with electron blocking ability (*i.e.* low electron affinity) or ETL with hole-blocking ability (*i.e.* deep valence band energy) are preferred for an efficient PeLED. Successful high efficiency demonstrations in solar cells fueled interest in perovskites for light emission applications. Thus, the early reports on 3D perovskite PeLEDs employed the basic device structure from solar cells, with $\text{CH}_3\text{NH}_3\text{PbI}_3$ perovskite infiltrated in to mesoporous TiO_2 ,^[4] with spiro-OMeTAD functioning as the HTL and the ITO and TiO_2 providing the electron injecting contact and ETL, respectively (Figure 10a). Significant electroluminescence ($7.1 \text{ W sr}^{-1} \text{ m}^{-2}$), EQE (0.48%), and exceptionally low turn on voltage (comparable to the emitter bandgap, *i.e.* 1.5 eV) was shown with this approach.^[4, 5] Despite the lack of carrier confinement capability in the solar cell configuration, the superior EQE and low turn on voltage suggested significantly low non-radiative losses of the materials. When $\text{CH}_3\text{NH}_3\text{PbI}_3$ was substituted with $\text{CH}_3\text{NH}_3\text{PbBr}_3$, the bandgap and consequently the emission wavelength of the PeLED could be altered to the visible region (*i.e.* 2.5 eV).^[99]

Inorganic oxide semiconductor materials (*i.e.* ZnO , TiO_2) have significant advantages when employed as the ETL, such as its moisture and thermal stability. However, their electron affinity is considerably high, which can hinder the electron injection to the emitter, especially

when high band gap $\text{CH}_3\text{NH}_3\text{PbBr}_3$ emitter is used. Surface modifiers could be introduced to initiate the formation of surface dipoles and consequently increase the work function of oxide semiconductor to facilitate better carrier injection in to $\text{CH}_3\text{NH}_3\text{PbBr}_3$. Ethanolamine (EA) could be employed as compact TiO_2 surface modifiers resulting in an increase of 0.3 eV in the TiO_2 work function. The use of EA as compact TiO_2 surface modifiers (ITO/ TiO_2 /EA/ $\text{CH}_3\text{NH}_3\text{PbBr}_3$ /SPB-02T/ MoO_3 /Au) resulted in turn on voltage reduction from 4.5 V to 3.5 V and EQE enhancement from 0.026% to 0.051% at 5.8 V.^[99] Efforts to further enhance the EQE were focused on increasing the electron mobility by using ZnO as ETL, and facilitating charge injection in to the emitter by lowering the work function of the ETL through surface modifiers (e.g. poly(ethylenimine); PEI), and using HTL with high electron affinity (TFB) to block the electron flow. These device architectures (**Figure 11a**) resulted in brightness and EQE as high as $28 \text{ W sr}^{-1} \text{ m}^{-2}$ and 3.5% at 2.2 V for devices with $\text{CH}_3\text{NH}_3\text{PbI}_3$ as the emitter.^[100] When $\text{CH}_3\text{NH}_3\text{PbBr}_3$ was employed as the emitter, EQE of 0.8% with brightness of 20000 Cd m^{-2} could be attained at 2.8 V (Figure 11b). The turn on voltages of these devices are comparable with the bandgap of the emitter (*i.e.* 1.5 eV and 2.5 eV for $\text{CH}_3\text{NH}_3\text{PbI}_3$ and $\text{CH}_3\text{NH}_3\text{PbBr}_3$, respectively).^[100] The emission spectra with various applied voltage are also consistent with the emitter bandgap (Figure 11c). The high brightness at significantly low voltage indicated small energy loss from carrier transport and carrier injection to the emitter as well as superior carrier confinement in the emitter layer.

On the other hand, the first report of electroluminescence with HTL/perovskite/ETL configuration was on ITO/PEDOT:PSS/emitter/poly(9,9-dicetylfluorene)(F8)/Ca/Ag structure which resulted in turn on voltage of 1.5 V and 3.3 V with EQE of 0.23% and 0.1% for $\text{CH}_3\text{NH}_3\text{PbI}_3$ and $\text{CH}_3\text{NH}_3\text{PbBr}_3$ respectively.^[5] Due to formation of on-chain keto defects in F8 under applied bias in air, atomic layer deposition of Mg doped ZnO could be an alternative to improve device stability. Mg addition to ZnO facilitated an increase in the work function by 0.3 eV, easing the injection of carriers in to the emitter.^[101] Tuning the work function of

HTLs is also essential and been pursued by doping PEDOT:PSS with perfluorinated polymeric acid (PFI),^[102, 103] resulting in the ability to tune the work function of the PEDOT:PSS between the ranges of 5.2 eV and 5.95 eV (SOCF). This resulted in enhanced carrier injection in the ITO/SOCF/CH₃NH₃PbBr₃/TPBi/LiF/Al device structure. The enhanced carrier injection resulted in turn on voltage reduction from 6.5 V to 4 V and 300-fold EQE improvement to 0.125%.^[102] In addition to minimizing the energy difference at the interfaces, balanced electron and hole injection in to the emitter is also crucial for PeLED efficiency. Tailoring the electron and hole injection into the emitter via altering the composition of bipolar transporting material (*i.e.* PVK:PBD blend) in ITO/PEDOT:PSS/CH₃NH₃PbBr₃/PVK:PBD/BCP/LiF/Al device structure ,resulted in enhanced EQE from 0.2% to 0.48%.^[87]

3.1.2. Engineering the Emitter Layer Towards High Efficiency PeLEDs

Perovskite emitters integrated in PeLEDs can take the form of films fabricated from 3D, lower dimensionality layered materials, or nanostructured materials. Requirements for the emitter layers include dense, defect and pin-hole free layers that facilitate charge injection and facile light emission. To this effect, besides solution processed or evaporated perovskite thin films, polymer-perovskite blends, closely-packed nanocrystals or quantum dots have been explored. The following sections will elaborate on efforts to boost the PeLED performance from engineering materials and processes of depositing the emitter layer.

3.1.2.1. 3D Perovskite Thin Film-based PeLEDs

Besides the energy band alignment to promote balance carrier injection, the morphology and crystal quality of the emitter also plays important roles in PeLED. One of the main advantages of using thin films of 3D perovskites as emitter materials is their excellent electrical properties, which can offer very efficient charge carrier transport. However, pinholes in the

film result in substantial decrease of the overall conductivity, current leakage, and non-radiative recombination paths that reduce the efficiency of the PeLEDs. Different solution deposition routes to enhance the coverage of the emitter, such as altering crystallization rates and inducing nucleation have been reported.^[40, 104] By adding acid to the precursor solution (*i.e.* HBr) the concentration for supersaturation increases, which lowers the crystallization rate and consequently leads to the formation of a thinner film with a better surface coverage. Another approach to improving film quality relies on additives that reduce the solubility of the precursors (anti-solvents), induce fast nucleation resulting in reduced grain size and increased uniformity and coverage of the perovskite film (**Figure 12**). Addition of various anti-solvents to promote nanocrystal pinning (NCP) to the CH₃NH₃Br₃ coupled with excess CH₃NH₃Br₃ added to the films resulted in record EQEs and current efficiencies of 8.53% and 42.9 Cd m⁻² respectively in a device configuration comprising of SOCP/CH₃NH₃PbBr₃/TPBi/LiF/Al.^[40] The enhancements were attributed to reduced carrier diffusion lengths and increased spatial carrier confinement in the emitter related to reduced grain sizes and to the passivation of atomic Pb defects with excess CH₃NH₃PbBr₃ added to the precursor solution.^[40]

Despite its promising research progress, the thermal stability of the organic-inorganic perovskite halide is the main issue which resulted in device degradation and efficiency drop off due to heating at high current densities.^[5] Besides the CH₃NH₃PbBr₃ family, thin film CsPbBr₃ based PeLEDs (ITO/PEDOT:PSS/CsPbBr₃/F8/Ca/Ag) have recently been reported. These devices displayed turn on voltage of 3 V with an EQE of 0.01% at 400 Cd m⁻²; with the relatively low performance of the devices being attributed to the presence of pinholes in the emitter layer.^[32] Similar to the above mentioned instance of adding stoichiometrically higher amounts of CH₃NH₃Br₃; in this instance, higher amounts of CsBr displayed enhancements of up to 150% in current efficiency. This observation was attributed to reduced defects densities in CsPbBr₃. The EQE could be boosted further to 0.026% and the turn-on voltage could be

reduced further to 2.5 V by using PFI doped poly-TPD as the hole transporting material, again highlighting the critical role played by the interface materials in enhancing the device performance.^[103]

3.1.2.2. Polymer-Perovskite Blend Thin Films

Pin-holes in the perovskite films present pathways for electrical shorts between the HTL and ETL resulting in high leakage currents and significantly reduced current efficiencies. To block the current leakage through pin holes, an insulating polymer (such as poly(imide); PIP) could be blended with the emitter layer to continuous polymer-perovskite films. With ITO/PEDOT:PSS/CH₃NH₃PbBr₃:PIP blend/F8/Ca/Ag device configuration (**Figure 13a**), reduced current density (Figure 13b), reduced turn on voltage, and enhanced of EQE up to 2 order of magnitudes was achieved.^[38] The superior EQE value was attributed to the low current density and high brightness for devices with PIP. Other insulating polymer, such as poly(ethyleneoxide) (PEO), has also been used to passivate the pin holes in the emitter film which resulted in reduced current density and therefore increased EQE up to 1.1% with 2.6 V turn on voltage.^[39, 105] Low current density accompanied with high brightness and EQE enhancement indicated that pin-holes on the emitter layer could be passivated with insulating materials.

3.1.2.3. Perovskite-based Nanoparticles (NPs) and Nanoplatelets (NPLs)

As described in the earlier sections, highest PLQY obtained in thin films vs NPs were 35 and 90%, respectively. Enhanced PLQY is caused by confinement of the charge carriers within the NP or NPL resulting in increased radiative recombination efficiencies. As described in the previous section, nanostructured perovskites can be formed from 3D and layered perovskites using a variety of techniques including hot injection, adding precursors to low-solubility solvents, ligand-assisted reprecipitation; followed by purification prior to film formation.

Although NPs yield very high PLQY in solution, the quantum yields upon film formation drop precipitously. This drop in PLQY may be the effect of increased surface states that hinder radiative recombination. If during film formation, the NPs fail to form continuous films, charge injection and transport would suffer in addition to the increased leakage currents. Nevertheless, PeLEDs of $\text{CH}_3\text{NH}_3\text{PbBr}_3$ NPLs were successfully demonstrated in a ITO/PEDOT:PSS/ $\text{CH}_3\text{NH}_3\text{PbBr}_3$ /PVK:PBD/BCP/LiF/Al device configuration resulted in maximum EQE of 0.45% at 6.6 V with turn on voltage of 3.8 V.^[87] Besides the use of NPLs as emitters, $\text{CH}_3\text{NH}_3\text{PbBr}_3$ NPs with size <10 nm were also demonstrated in a ITO/PEDOT:PSS/ $\text{CH}_3\text{NH}_3\text{PbBr}_3$ /TPBi/CsF/Al device configuration (**Figure 14**), to yield 1.1% EQE, luminescence of 410 Cd m^{-2} with a 2.9 V turn on voltage.^[106] Although thus far these are the only two reports successfully integrating organic-inorganic perovskite halide nanostructures into LEDs, significant progress is expected in this field due to the higher PLQY of nanostructures compared with thin films, and also through leveraging QLED approaches for high performance LEDs.

3.2. Light-emitting Transistors and Electrochemical Cells

Electroluminescence has also been observed on the 150 nm thick $\text{CH}_3\text{NH}_3\text{PbI}_3$ based field effect transistor (FET) at low temperatures (78-178 K).^[6] Bottom gate bottom contact FET configuration was employed with thermally oxidized SiO_2 , Si(p++), and Au as the dielectric layer, gate contact, and source-drain contact respectively. As some reports have shown ionic conductivity in $\text{CH}_3\text{NH}_3\text{PbI}_3$,^[107, 108] low temperatures are thought to have been crucial to impede ionic transport that may lead to n-type or p-type self-doping. The $\text{CH}_3\text{NH}_3\text{PbI}_3$ based FET emits light if they are operated in the ambipolar regime where balanced charge injection was achieved. The emission spectra are consistent with the $\text{CH}_3\text{NH}_3\text{PbI}_3$ bandgap, signifying the direct recombination of injected electrons holes in the emitter. Furthermore, the carrier injection and recombination could be easily altered by adjusting the biasing conditions (*i.e.*

drain voltage and gate voltage).^[6] This opens up the possibility for use of perovskites for high brightness PeLEDs and potentially an avenue towards realization of electrical injection lasers.

Another device configuration reported is that of light-emitting electrochemical cells (LEC). Here, perovskite emitter layer is sandwiched between two electrodes with similar work functions, such as ITO / Ag (**Figure 15a**),^[105] ITO / InGa,^[39] and ITO / Au.^[109] The feasibility of using ETL or HTL free device structure was attributed to the nature of perovskite as ionic conductor. In the presence of electric field, the ions will drift, creating a p-i-n or n-i-p structure within the perovskite layer, thus facilitating carrier confinement in the emitter (Figure 15b).^[39] EQE as high as 1.1% at 20,000 Cd m⁻² with turn on voltage of 2.6 V could be achieved with ITO/CH₃NH₃PbBr₃:PEO blend/Ag nanowire device structure. Device fabrication in ambient conditions was also demonstrated, signifying the stability of CH₃NH₃PbBr₃:PEO blend layer towards moisture and air (Figure 15c). Despite the much simpler device structure, good EQE with turn on voltage similar to the emitter bandgap signify the low non radiative recombination nature of the devices.

3.3. Mechanisms and Photophysical Properties of Light-emitting Devices

Despite the rapid development of perovskite solar cells and PeLEDs, the mechanisms influencing their optoelectronics performance are still under intense investigation. Insights into basic processes such as charge injection, transport, and recombination are necessary for an optimum device design, and a combination of reported electrical and optical techniques to probe energy and charge transfer processes would be essential for further advances in this field.

3.2.1. Working Mechanisms of PeLEDs

The charge transport characteristics of the emitter plays, along with the optimization of the interfaces, the key role in the determination of the device external quantum efficiency. A

standard LED, regardless of the nature of its active material, generates light (photons) from the radiative recombination of an electron and a hole. Similar concentrations for both charge carriers are thus necessary to maximize the efficiency of the device. Ambipolar materials, with good transport properties for both electrons and holes, make the most suitable candidates. From this point of view, perovskites are particularly suitable due to their free charge carriers-dominated transport^[110, 111] with long and balanced charge carrier diffusion lengths.^[9, 10] Indeed, this is one of the most attractive properties of metal halide perovskites, which has been crucial to understand the impressive success of perovskite photovoltaics. The first charge transport reports on thin film $\text{CH}_3\text{NH}_3\text{PbI}_3$, presented diffusion lengths larger than 100nm.^[9, 10] These values have been matched, or even improved, by other perovskites films such as FAPbI_3 .^[42] Single crystal systems ($\text{CH}_3\text{NH}_3\text{PbI}_3$, $\text{CH}_3\text{NH}_3\text{PbBr}_3$ and $\text{CH}_3\text{NH}_3\text{PbCl}_3$) display yet longer charge carrier diffusion lengths, in the order of tens and hundreds of micrometers (**Figure 16a-b**).^[112, 113]

These properties have two direct repercussions in the pursuit for high performance PeLEDs. On the one hand, the good electrical transport properties are crucial for achieving large and balanced charge carrier densities.^[114] On the other hand, large diffusion lengths generally imply low defect density in the material, which reduces the non-radiative trapping paths. As a result, time resolved photoluminescence decay (TR-PL) measurements used to calculate diffusion lengths, are good estimations of the recombination process and the material defect density. The lifetimes extracted from TR-PL show a bimolecular-like decay for the slower component in $\text{CH}_3\text{NH}_3\text{PbI}_{3-x}\text{Cl}_x$ ^[31] samples, in good agreement with those obtained from terahertz measurements,^[115] which is another indicator of low non-radiative recombination. The reduction of the defects through precursor engineering, used to enhance the PeLEDs efficiency in CsPbI_3 based devices, was also reflected in the increase of the PL lifetimes.^[32]

In contrast, Cho *et al.* claim to reduce the diffusion length of the perovskite (to 67 nm) in order to improve the performance of the devices, reasoning that the reduced grain sizes generate strong spatial confinement which enhances the radiative recombination. They control the crystal size of a 3D $\text{CH}_3\text{NH}_3\text{PbBr}_3$ film by means of a variation of the precursor concentration. However, the reported PL lifetime of these samples gradually increased from 12.2 to 51.0 ns as the crystal size is enlarged.^[40] The highest current efficiency in this report (42.9 Cd A^{-1}) is achieved with a 1.05:1 mixture of $\text{MABr}:\text{PbBr}_2$, which generates the longest PL lifetime as well (51.0 ns). The optimum configuration is thus unclear; although the authors claim that reduced grain sizes result in a better radiative performance, the increased number of grain boundaries should enable additional non-radiative paths. All in all, with an accurate electron and hole blocking capacity of the respective contacts, the larger diffusion length of the emitter should generally result in better performance; not only due to the better charge transport, but also due to the reduction of the defect concentration which can activate non-radiative recombination pathways.

Some reports seem to indicate significant ion conductivity in metal halide perovskites.^[107, 108] Yang *et al.* reported higher ionic conductivity than electronic one for FAPbI_3 and $\text{CH}_3\text{NH}_3\text{PbI}_3$, which is attributed to a high native ionic disorder in the perovskite.^[108] A theoretical study by Eames *et al.* extracted activation energies of $\sim 0.6 \text{ eV}$ for vacancy-assisted migration of iodide ions in $\text{CH}_3\text{NH}_3\text{PbI}_3$.^[107] The estimation of the activation energy is even lower ($\sim 0.1 \text{ eV}$) in the calculations reported by Azpiroz *et al.*^[116] This may have an effect in the operational stability of the devices, mainly due to the large electric field resulting from a very thin perovskite film exposed to the large applied voltages in PeLEDs (see Outlook & Conclusions section). However, it also opens the possibility of light-emission applications with different working mechanism.

The presence of ionic conduction (**Figure 17a**) concurrent to the electronic one enables the possibility of the aforementioned light-emitting electrochemical cells. Although

most of the reported PeLEDs use high work function anodes and low work function cathodes to tune the charge injection, Zhang *et al.* presented a work where the device uses two high work function electrodes with an almost symmetric architecture (MoO₃/Au and PEDOT:PSS) as contacts.^[109] This configuration, similar to a classic light-emitting electrochemical cell (the device reduces its dependence on the difference in work function of the electrodes^[117]), enables the electroluminescence from both forward and reverse biases (Figure 17 b-c). Based on their use of a mixed halide perovskite (CH₃NH₃PbI_{3-x}Br_x), they interpret the shift of the emission spectrum as a motion of I⁻ ions with an ionic conductivity of 10⁻⁸ S cm⁻¹, with some extra contribution to the current by the electronic conductivity as well. The concept of light-emitting electrochemical cell based on perovskite was previously used by Aygüler *et al.*, however in this work, the employed electrodes were not symmetric (Al and PEDOT:PSS), and the perovskite nanoparticles were embedded in an electrolyte matrix (LiCF₃SO₃ and TMPE), instead of utilizing the ionic conductivity of the perovskites.^[118] With this approach, they present a luminance of ~2 cd m⁻² at low driving currents. Despite the lower performance of current perovskite light-emitting electrochemical cells, the simplicity of the structures, the relaxation of the thickness requirements and the flexibility in the contact choice (which enables the use of more air stable contacts) make these devices very attractive for future applications.

3.2.2. Optical and Electrical Interfacial Losses

Maximizing the light emission requires an efficient engineering of the multiple layers of the devices to control charge carrier injection and light extraction. Interfaces also influence the self-assembly, structure, stability and color purity of active layers, and play a critical role in long term stability with failure mechanisms attributable to interface defects. This aspect becomes even more important with new perovskite materials being developed, where exciton binding energy shifts, band bending at the interface, charge transport in the contact layers

have to be reconsidered. Therefore, a judicious choice of the contact materials is a crucial step to optimize the device performance and minimize the losses. Interfacial losses in PeLEDs can be divided, depending on their origin, in optical and electrical losses (**Figure 18**). Differences in the refractive index (n) between each film may result in total internal reflection at the interfaces, thus trapping light in the emissive layer. To reduce such losses, strategies employing index matching of the emissive layer and the substrate^[110] have been successfully applied to inorganic LEDs. Ordered structures, such as pyramidal or lens arrays, can improve the total light output as well.^[111] The coupling of the radiation dipoles to the plasmon states of the metal cathode is another loss which could strongly decrease the emission efficiency, and can be minimized by a thicker transport material.^[110]

In addition to non-radiative recombination processes such as Auger and trap-assisted, electrical losses related to the interfaces (Figure 18b) include high interfacial injection energy barrier which reduces the efficiency by increasing the required voltage; non-radiative recombination in surface states which reduces the PLQY; and imbalanced carrier injection which can result in accumulation of carriers out of the emissive layer, especially at high brightness and bias.^[112] The control of the interfacial energetics is thus essential to minimize these losses, since it can gradually reduce the injection barrier via a matched energy architecture with improvements in current efficiency, EQE, and brightness,^[9, 10] and control the carrier injection. At the same time, a shallow LUMO of the HTL can block electrons and vice versa for ETL, thus reducing the leakage; and the surface treatments can passivate the surface traps originating from non-radiative recombination. Naturally, tailoring the ETL and HTL layers has been one of the main sources of PeLED performance improvement to date, as expanded in the previous section. Yu *et al.* applied this approach to tune the electron injection layer, TiO₂, with an ethanolamine solution.^[99] The resulting interface, originated an interfacial dipole which reduced the electron injection barrier and the surface recombination.

A similar approach was followed by Wang *et al.*^[100] In their work, a poly(ethylenimine) interlayer tuned the energetic alignment of the ZnO/MALI interface by lowering the cathode work function, thus reducing the turn-on voltage to 1.3 V.

4. Lasers and Optical Gain from Halide Perovskites

Since the invention of the semiconductor solid-state laser in the mid-20th century, lasers have become a ubiquitous part of our daily lives. Solution-processed gain media (e.g., organic polymers and colloidal quantum dots) offer the advantages of low-cost sustainable production and applicability to flexible and wearable optoelectronic devices. The entrants into this field are the halide perovskites. The realization of ultralow threshold room temperature (RT) amplified spontaneous emission (ASE) and lasing from CH₃NH₃PbX₃ (X = Cl⁻, Br⁻, and I⁻) polycrystalline thin films in early 2014 amidst the solar-cell efficiency race launched a new light emission direction for the 3D perovskites.^[2] This can be traced to the tantalizing possibility of realizing electrically-driven lasing through harnessing the long range ambipolar charge transport properties of CH₃NH₃PbI₃. In the subsequent sections, we will review the key works on the optical gain from perovskite polycrystalline thin films, micro/nano-structures and colloidal perovskite nanocrystals and discuss their gain mechanisms. **Table 2** summarizes the recent major findings and key parameters of ASE/lasing from organic-inorganic and all-inorganic perovskite gain media.

4.1. ASE/lasing from Perovskites

4.1.1. ASE/lasing from Perovskite Thin Films

Optically-pumped RT ASE and lasing from was first demonstrated in solution-processed organic-inorganic 3D halide perovskites (CH₃NH₃PbX₃, X = Cl⁻, Br⁻, or I⁻) 65 nm-thick thin films.^[2] Reported threshold fluence for ASE was as low as $(12 \pm 2) \mu\text{J cm}^{-2}$ (corresponding to a carrier density of $1.7 \cdot 10^{18} \text{ cm}^{-3}$) and is comparable to the state-of-the-art solution-processed

gain media (e.g. poly(9,9-dioctylfluorene-co-9,9-di(4-methoxyphenyl)fluorene, F8DP, $\sim 6 \mu\text{J cm}^{-2}$, colloidal CdSe/CdS nanoplatelets films $\sim 10 \mu\text{J cm}^{-2}$). The relatively low ASE threshold can be attributed to their large absorption coefficients, small capture cross-sections of trap states, low bimolecular recombination and slow Auger recombination properties.^[2, 119] More importantly, $\text{CH}_3\text{NH}_3\text{PbI}_3$ is an extremely durable gain medium that can yield an invariant ASE intensity with only a 0.2% standard deviation about its mean intensity under 26 hours of sustained irradiation (*i.e.*, $\sim 10^8$ laser shots) with a 1 kHz Ti-sapphire regenerative amplifier. Such excellent photostability corroborates that solution-processed organic–inorganic halide perovskites is a robust, high performance gain medium. By straightforward combination of the different precursors, the composition of these perovskite films could be easily tuned to achieve broad wavelength tunability from ~ 390 nm to 790 nm (**Figure 19a**). Furthermore, by sandwiching $\text{CH}_3\text{NH}_3\text{PbI}_3$ perovskite thin films within a cavity composed of a thin-film ($\sim 7 \mu\text{m}$) cholesteric liquid crystal (CLC) reflector and a gold back-reflector (Figure 19b), the threshold fluence for ASE in the perovskite film can be reduced by at least two orders of magnitude (Figure 19c).^[120]

Deschler *et al.*^[31] demonstrated RT optically pumped lasing from $\text{CH}_3\text{NH}_3\text{PbI}_{3-x}\text{Cl}_x$ in a micro-cavity constructed using a sandwiched perovskite film between a commercial Bragg reflector mirror and a thin gold layer (with a threshold of $0.2 \mu\text{J}$ per pulse using 400-ps pump pulse; Figure 19d-e). Perovskite lasing can also be controlled by using the approach of in-plane structuring of perovskite thin films on 2D patterns. Very recently, Saliba *et al.*^[121], by evaporating perovskite film onto a nanoimprinted polymer resist, fabricated the perovskite distributed feedback (DFB) lasers with very low thresholds of $\sim 0.32\text{--}2.11 \mu\text{J cm}^{-2}$ (using 1-ns pump pulse). The lasing can be tuned between 770 and 793 nm by simply varying the grating periodicity (Figure 19f-g). Perovskite films with DFB cavities have huge potential as inexpensive, error-free, widely tunable, easily manufactured single mode lasers. Organic-inorganic halide perovskites are thus a new class of robust solution-processed optical gain

media with highly desirable characteristics.

4.1.2. Lasing from Perovskite Micro/nano-structures and Colloidal Perovskites

Single micro/nanocavity perovskite lasers have also attracted significant attention given their interesting physical morphologies for possible applications in optoelectronic devices. Xing *et al.*^[2] first realized RT lasing from a $\text{CH}_3\text{NH}_3\text{PbI}_3$ crystal of size several tens of micrometers from solution processed drop-casted thin films (**Figure 20a-b**). In contrast to polycrystalline thin films, low-dimensional single-crystal micro-/nanostructures exhibit higher crystalline quality which in turn implies longer carrier diffusion length, lower defect densities, and reduced scattering for lower threshold applications. Their faceted structures also serve as a resonant optical cavity for light amplification. As such, they are attractive for potential applications as miniaturized solid-state lasers in integrated optoelectronic chips.

Presently, RT lasing has been achieved in several types of individual organic-inorganic perovskite micro-/nanostructures. For example, Zhang *et al.*^[36] had used a vapor chemical deposition method (Figure 20c) to synthesize highly crystalline organic-inorganic perovskite $\text{CH}_3\text{NH}_3\text{PbI}_{3-x}\text{X}_x$ ($\text{X} = \text{I}^-$, Br^- , and Cl^-) platelets on muscovite mica with nanoscale thickness (10–300 nm) and edge length of several to tens of micrometers. The side faces of well-defined polygonal perovskite form an in-plane built-in whispering gallery mode (WGM) micro-resonator that ensures adequate gain and efficient optical feedback for low-threshold optically pumped in-plane lasing, with reported Q-factors as large as ~ 1300 . These planar platelets could also be easily transferred onto conductive platforms such as Si, Au, indium tin oxide, etc., suitable for chip integration. Similarly, Liao *et al.*^[122] also reported to have realized the WGM lasers from $\text{CH}_3\text{NH}_3\text{PbBr}_3$ single crystal square microdisk prepared using a facile one-step solution self-assembly method with lasing thresholds as low as $\sim 3.6 \mu\text{J cm}^{-2}$ using 120-fs pump excitation (Figure 20d).

Due to their ultra-compact physical sizes, highly localized coherent output, and efficient waveguiding, nanowire (NW) lasers are regarded as promising building blocks for fully integrated nanoscale photonic and optoelectronic devices. Each NW can act as a waveguide along the axial direction, while the two end facets constitute a Fabry-Perot cavity for optical amplification. Since the seminal work by Yang's group of achieving the RT ultraviolet lasing from ZnO NWs in 2001,^[123] optically pumped lasing has been realized in a few kinds of NWs in the ultraviolet to near-infrared regions. One of the main obstacles that hinder the potential applications of semiconductor NW lasers is that the lasing requires a high threshold carrier density. In this regard, Zhu *et al.*^[124] very recently demonstrated that low temperature solution processed single-crystal organic-inorganic perovskite nanowires are also ideal candidates for NW lasing (Figure 20e-f)^[3] with very low RT lasing threshold of $\sim 220 \text{ nJ cm}^{-2}$ (corresponding to a threshold charge carrier density of $1.5 \cdot 10^{16} \text{ cm}^{-3}$) and high Q-factor (~ 3600). Similar organic-inorganic perovskite nanowire lasers were also demonstrated using a vapor-phase-synthesis method (Figure 20g-h).^[71] All these examples signify the great potential of this fledging field.

Colloidal semiconductor nanocrystals (NCs) are also another promising class of optical gain media possessing attractive properties of wide size-dependent color tunability and spectrally narrow gain profiles and ease fabrication properties.^[125, 126] Very recently, all-inorganic colloidal NCs of cesium lead halide perovskites (CsPbX_3 , $\text{X} = \text{Cl}^-$, Br^- , and I^-), have emerged as a new class of colloidal NCs optical gain media.^[127-129] that are clearly superior to the traditional metal-chalcogenide nanocrystals. These perovskite nanocrystals deliver prominent optical gain signatures that combines the advantages of both quantum dots and halide perovskites: namely, good photochemical and oxidative stability even without shell coating (such as CdS used in traditional CdSe/CdS quantum dots), high PL quantum yield (up to 90%), narrow emission linewidths of 70–100 meV, precise and continuous tuning emission wavelength peaks from 410 to 700 nm via compositional control (mixed halide Cl/Br and Br/I

systems) and effect of quantum confinement. For example, using cubic-shaped colloidal cesium lead halide perovskite NPs (CsPbX_3 , $\text{X} = \text{Cl}^-$, Br^- , and I^-) with mean size of $\sim 9\text{--}10$ nm, Kovalenko's^[129] and Sun's^[127] groups demonstrated the RT stimulated emission in the entire visible spectral range (440–700 nm), respectively (**Figure 21a**). The ASE threshold from CsPbX_3 NPs thin film was able to be reach as low as 5 ± 1 uJ cm^{-2} using a 100-fs pump pulse (1 KHz).^[129] Spherical and ring WGM microlasers were demonstrated by conformally coating CsPbX_3 NPs on the surface of silica microsphere (Figure 21b) or on the inner wall of microcapillary tube (Figure 21c), respectively. Aside from the aforementioned one-photon excitation, ultra-air- and photostable RT ASE in surface-passivated CsPbBr_3 NPs films via two photon absorption process were also demonstrated by Pan *et al.*^[128] This further expands the potential application of these NPs in nonlinear photonics.

4.2. Mechanisms of Optical Gain in Organic-Inorganic Perovskites

As a hybrid compound, the properties of the $\text{CH}_3\text{NH}_3\text{PbI}_3$ are often a matter of debate, particularly on whether the stimulated emissions are driven by excitonic recombination or free electron–hole plasma recombination that can respectively happen in organic and inorganic semiconductors. This could also be attributed to the wide range of reported exciton binding energies (*i.e.*, <10 meV to ~ 50 meV).^[130] A recent comprehensive investigation by Saba *et al.*^[119] on the steady state and transient PL intensities of $\text{CH}_3\text{NH}_3\text{PbI}_3$ (with photoexcited carrier densities n_0 spanning 10^{16} - 10^{19} cm^{-3}) would finally shed light on this issue. It was found that a predominant population of free carriers with negligible bound excitons was generated even at $n_0 < 10^{18}$ cm^{-3} . At a higher photoexcited carrier densities ($n_0 > 10^{18}$ cm^{-3}), the carrier dynamics are forced into a competition between the nonlinear processes of radiative bimolecular recombination of the free electrons and holes and the non-radiative Auger recombination. Although the bimolecular recombination rate is $\sim 3\text{--}4$ orders lower than that predicted by the Langevin model,^[115, 131] with no other relaxation pathways available, the two-

particle radiative bimolecular recombination would still be more favorable than the three-particle Auger recombination. The latter only dominates at excitations $>10^{19} \text{ cm}^{-3}$.^[119] Interestingly, the Auger rates detected ($\sim 10^{-28} \text{ cm}^6 \text{ s}^{-1}$)^[115, 119] are comparable to that of strongly confined semiconductor colloidal quantum dots. Band filling by the free-electron hole plasma that manifests as the Burstein-Moss effect^[111] increases the Coulombic screening of the photogenerated electron-hole pairs and decreases the exciton binding energies. The carrier accumulation at the band edge provides the necessary population inversion condition needed for attaining light amplification. Hence, stimulated emission out-competes the multi-particle processes^[2, 119] the at electron-hole plasma densities of $1\sim 3\cdot 10^{18} \text{ cm}^{-3}$.

In contrast to the electron-hole plasma recombination mechanism in the optical gain of $\text{CH}_3\text{NH}_3\text{PbX}_3$ perovskites, the origin of stimulated emission in CsPbX_3 NPs can be clearly ascribed to the recombination of bi-excitons. These bi-excitons possesses a binding energy of $\sim 50 \text{ meV}$ – derived based on the energy separation between exciton and bi-exciton peak positions (Figure 21d-e)^[127]. The large bi-exciton binding energy was found to drive the thermally stable RT bi-excitonic lasing and also help reduce the linear absorption losses.

5. Outlook

Organic-inorganic hybrid perovskites have the potential to replicate the breakthrough performances in photovoltaics and transform the field of light emission. Although the present device performances (quantified by brightness and current efficiency) still lag behind technologies such as OLEDs and QLEDs, the surge achieved in merely two years promises to emulate the established technologies. The basis of this projection is the remarkable intrinsic properties these hybrid perovskites possess, as well as their facile structural and photophysical tunability.

Smooth interfaces between the perovskite emitter and the electron/hole transport layers (or electrodes) will be paramount for good charge injection and avoidance of parasitic non-radiative recombination from surface defects (*i.e.* pinholes). Likewise, the formation of metallic Pb has also been identified as major contributor to non-radiative losses.^[40] To promote efficient and balanced current injection, tailoring the band alignment of the devices through proper selection of ETL and HTL, surface dipolar modification, and doping can be pursued. Additionally, introduction of a very thin film of insulating high band gap materials (e.g. poly(methylmethacrylate); PMMA) between the electrode and emitter layers, may help reduce the concentration of a specific charge carrier, and thus promote balanced charge injection.^[132] The minimization of optical losses by employing light-coupling techniques or refraction index matching between device layers can be followed, similar to the approaches employed in current lighting technologies. Chemical and morphological control during thin film fabrication is thus key to optimal light-emission, and have already been substantially improved with a number of process^[37] and solvent engineering approaches. High-efficiency perovskite solar cell modules (*i.e.* >12%) have been achieved via various solution-based processing techniques (e.g. printing, slot die coating, etc.), and it seems only matter of time that efficient light-emitting devices will leverage on these advances for large area applications. In fact, the first fully printed LED has already been demonstrated, displaying the highest

recorded brightness ($\sim 21,000 \text{ cd m}^{-2}$), albeit at a low EQE ($>1\%$).^[105] Despite the possibility of transferring fabrication techniques between solar cell modules and PeLEDs, lasers several restrictive characteristics for light emission, such as very thin homogeneous emitter layers (to promote radiative recombination), would require new processes/formulations to be developed for scalability. To date the largest PeLED fabricated had an area of 4 cm^2 .^[40]

On the other hand, nanostructured perovskites like colloidal NPs have displayed remarkable luminescence properties with quantum yields approaching 100% and high color purity. Despite much higher quantum yields and exciton binding energies than observed in films, the few perovskite QD-devices reported to-date,^[106, 133] have delivered lower efficiencies and brightness than thin film-based devices. Capping ligands, although effective in controlling the crystallization kinetics and size of the NPs, may hinder the formation of smooth thin films. Their unfavorable wettability restrict the formation of smooth, pinhole-free films, and often fastidious purification steps are required to remove excess ligands. In turn, this may result in nanostructure coalescence (due to destabilization), and subsequent photoluminescence quenching due to grain growth.^[134] Device efficiencies can be seriously affected by poor electrical injection due to remnant surface ligands. Although other approaches involving the use of polymer matrices to embed the NPs have been proposed, the challenge remains to look into novel strategies to fully utilize the extraordinary properties of nanostructured perovskites in light-emitting devices. The amalgamation of confinement strategies offered by NPs and high charge injection offered by thin films, have resulted in the most efficient PeLED (CE of 42 cd A^{-1} , EQE $\sim 8.5\%$),^[40] where radiative recombination was significantly enhanced through confinement of charge carriers in small grains within a thin film architecture. Further improvements in device performances would need to address essential questions regarding intrinsic material properties, basic physical processes occurring within the perovskite material and optoelectronic devices. For example, the dominant charge transport mechanisms,^[135] or differences in PL emission originating from nanocrystals^[113, 136]

and thin films^[2, 4] of the same perovskite emitter need to be reconciled. A deeper understanding of the working mechanisms will be crucial to identify the limiting factor, and thus key to improve device performance.

Besides device performance enhancements, addressing the stability and long-term reliability of the materials and devices is paramount. Despite promising results obtained for solar cells by employing carbon films as protective layers (>2500 h of operation),^[137] the use of opaque films are not feasible for light-emitting devices. Accelerated reliability tests at high relative humidity levels (75-80%) and wide range of temperatures (-30 to 70 °C) would allow the estimation of the device lifetime. Furthermore, appropriate device encapsulation strategies and control of the fabrication ambient (e.g. fabrication in dry rooms utilized for battery assembly) would be necessary. Complications also involve structural instability originating from self-heating effects at high current densities (during operation) or under constant illumination. Encouraging results were obtained to address the former, by applying squared voltage pulses the heat was allowed to dissipate between the pulses, and no significant device degradation was observed.^[5]

Along with stability, toxicity concerns would drive the need for lead replacement, especially with the susceptibility of perovskites to degrade in presence of moisture, leading to the formation of (water soluble) Pb species. This may seriously challenge the prospects of hybrid perovskite-based technologies, and although several Pb-free perovskite alternatives (e.g. replacement Pb with Sn or Bi) displayed promising photoluminescence properties, the oxidation of Sn^{2+} to Sn^{4+} (*i.e.* formation of p-type defects),^[138] or the low-conductivity of Bi perovskites,^[139] have raised new challenges. The use of inorganic cations (Cs^+) instead of the small organic CH_3NH_3^+ cations, already demonstrated extended ambient as well as thermal stability, while retaining the 3D perovskite structure. Also, lower-dimensional layered perovskites may be exploited due to their intrinsically higher structural stability compared to 3D perovskites. The larger structural freedom allows for functionalization with more tailored

chemical moieties, and improved moisture stability may be achieved through introduction of large hydrophobic molecules. Another challenging set of factors is the behavior of halide perovskites under electrical stress. Ionic migration under high electric fields have been noted for some 3D perovskites,^[107] may result in compositional changes and subsequent perovskite degradation under standard PeLED operation. Such ionic migration may be tackled by appropriate choice of injection layers (which can also act as ion blockers), or through operation under lower and pulsed electrical bias.^[5]

All the challenges outlined for PeLEDs would be applicable to lasers with the additional requirements of managing up to two order of magnitude higher carrier densities and intricate optical cavity design. Although ultralow ASE thresholds ($<10 \mu\text{J cm}^{-2}$) were demonstrated, optical pumping was done through femtosecond laser pulses that pack a high amount of optical power. Demonstration of optical amplification lasting 100 ns required temperatures of 220 K and below.^[140] The next challenge to be tackled for perovskites as a viable gain media would be to achieve ASE and lasing with nanosecond laser pulses and continuous wave (CW) pumping at room temperatures. Such demonstrations would need new perovskite materials designed to withstand heating from longer optical pump pulses, with higher absorption cross-sections, and decreased energy densities. Engineering of high Q optical cavities and high quality resonator cavities for loss compensation would also be essential to effect reduction in gain thresholds. Although optically pumped polariton lasing has been observed in the ZnO,^[141] GaAs,^[142] and GaN^[143] systems, perovskite polariton laser remains largely unexplored despite some early work in the mid-2000s.^[144, 145] The quantum confined systems offered by lower-dimensionality layered perovskites and nanostructures would be top candidates to be explored for polariton lasing since they would allow for gain build-up to occur at much lower carrier lasing thresholds and allow for potentially thresholdless lasing with highly optimized cavities.

Despite the success in achieving solution-processed optically pumped color-tunable lasing with relatively low fluence threshold, electrically-driven lasing remains a significant challenge. Several obstacles must be overcome, such as the very high current densities necessary to reach the threshold carrier density for ASE. As a reference, the largest current densities achievable in standard OLED configurations ($\sim 200\text{--}300\text{ A cm}^{-2}$) are significantly lower than the prerequisite values for optical gain ($>5\text{ kA cm}^{-2}$),^[119] and thus, the challenge would be to design new perovskite materials where the carrier density threshold for lasing is accessible. Moreover, heating effects must be reduced for electric laser devices, as the higher current injection densities can potentially degrade both the organic charge injection layers as well as the gain media. Careful materials design or device fabrication could overcome these challenges, e.g. through the use of all-inorganic perovskite NPs or lower-dimensional layered perovskites. For the device fabrication, electrically driven lasers using LETs configuration (rather than the conventional OLED structure) may be one promising direction.^[146] The underlying rationale is that the LET configuration allows for increased injected current densities. In addition, the LET configuration allows facile manipulation; the light-emitting medium can be placed far away from the source and drain electrodes in an attempt to reduce the non-radiative losses near the metal electrodes.^[147] Furthermore, resonator designs (e.g., LET architecture with a DFB resonator) and usage of high-quality single crystalline thin films or nanostructures (e.g., NWs, NRs, NPs, etc.) would augment the device performance by lowering the optically pumped lasing threshold even further.

6. Conclusions

The remarkable intrinsic properties and high degree of structural flexibility allow the potential for hybrid perovskites to go beyond academic curiosity and garner industrial interest. In particular the high quantum yields, narrow emission, high exciton binding energies, color tunability, and facile solution-processing at low temperatures should be exploited. Beyond

applications as emitters and optical gain materials, organic-inorganic hybrid perovskites may also be incorporated in currently existing technologies as replacement for phosphors. Identification of Pb-free light emitters would be a critical area of focus; and the leverage provided by nanostructuring and by layered perovskites to control binding energy and quantum yields holds the promise that the pursuit of Pb-free perovskite light emitters may be less challenging than that in photovoltaics. Emitter materials would need to be matched with selective contact materials and the diversity of heterojunctions, architectures, and processing conditions is certain to increase rapidly. En route towards commercialization, the optoelectronic properties including excitation dynamics, non-radiative recombination, the working principles and degradation mechanisms of hybrid perovskite materials in light-emitting devices would need to be well understood. The delicate interplay between the localized physics occurring within the various organic/inorganic building blocks, and the emergence of the delocalized behavior arising from such units embedded in a crystalline matrix, would need to be pursued. Buoyed by the successes in photovoltaics, it is reasonable to assume that research in perovskite optoelectronics will intensify in the foreseeable future ensuring a luminous future for organic-inorganic hybrid perovskites for applications in lasers and light-emitting devices.

Acknowledgements

We acknowledge the funding from National Research Foundation Singapore (NRF) Program #: NRF-CRP14-2014-03 and through the Singapore–Berkeley Research Initiative for Sustainable Energy (SinBeRISE) CREATE Program. T.C.S. acknowledges the support from NTU start-up grant M4080514; the Ministry of Education AcRF Tier 1 grant RG101/15, and Tier 2 grants MOE2013-T2-1-081 and MOE2014-T2-1-044. N.M. would like to acknowledge the funding support from NTU-A*STAR Silicon Technologies Centre of Excellence under the program grant No. 11235100003 and MOE Tier 1 grant RG184/14. Finally, the authors thank Koh Teck Ming, Ng Yan Fong, I.V. Kameshwar Rao, and Fadilah Nur Bte Jamuludin for their help in preparing the figures.

Received: ((will be filled in by the editorial staff))

Revised: ((will be filled in by the editorial staff))

Published online: ((will be filled in by the editorial staff))

References

- [1] NREL, **2015**, http://www.nrel.gov/ncpv/images/efficiency_chart.jpg.
- [2] G. Xing, N. Mathews, S. S. Lim, N. Yantara, X. Liu, D. Sabba, M. Grätzel, S. Mhaisalkar, T. C. Sum, *Nature Materials* **2014**, 13, 476.
- [3] H. Zhu, Y. Fu, F. Meng, X. Wu, Z. Gong, Q. Ding, M. V. Gustafsson, M. T. Trinh, S. Jin, X. Y. Zhu, *Nature Materials* **2015**, 14, 636.
- [4] O. A. Jaramillo-Quintero, R. S. Sanchez, M. Rincon, I. Mora-Sero, *Journal of Physical Chemistry Letters* **2015**, 6, 1883.
- [5] Z. K. Tan, R. S. Moghaddam, M. L. Lai, P. Docampo, R. Higler, F. Deschler, M. Price, A. Sadhanala, L. M. Pazos, D. Credgington, F. Hanusch, T. Bein, H. J. Snaith, R. H. Friend, *Nat. Nanotechnol.* **2014**, 9, 687.
- [6] X. Y. Chin, D. Cortecchia, J. Yin, A. Bruno, C. Soci, *Nat. Commun.* **2015**, 6.
- [7] C. Murawski, K. Leo, M. C. Gather, *Adv. Mater.* **2013**, 25, 6801.
- [8] Y. Shirasaki, G. J. Supran, M. G. Bawendi, V. Bulovic, *Nat Photon* **2013**, 7, 13.
- [9] S. D. Stranks, G. E. Eperon, G. Grancini, C. Menelaou, M. J. P. Alcocer, T. Leijtens, L. M. Herz, A. Petrozza, H. J. Snaith, *Science* **2013**, 342, 341.
- [10] G. Xing, N. Mathews, S. Sun, S. S. Lim, Y. M. Lam, M. Grätzel, S. Mhaisalkar, T. C. Sum, *Science* **2013**, 342, 344.
- [11] S. De Wolf, J. Holovsky, S. J. Moon, P. Löper, B. Niesen, M. Ledinsky, F. J. Haug, J. H. Yum, C. Ballif, *Journal of Physical Chemistry Letters* **2014**, 5, 1035.
- [12] P. Santhanam, D. Huang, R. J. Ram, M. A. Remennyi, B. A. Matveev, *Appl. Phys. Lett.* **2013**, 103, 183513.
- [13] Z. Hongping, L. Guangyu, Z. Jing, R. A. Arif, N. Tansu, *Display Technology, Journal of* **2013**, 9, 212.
- [14] M. Shukla, N. Brahme, R. S. Kher, M. S. K. Khokhar, *Indian J. Pure Appl. Phy.* **2011**, 49, 142.
- [15] L. Protesescu, S. Yakunin, M. I. Bodnarchuk, F. Krieg, R. Caputo, C. H. Hendon, R. X. Yang, A. Walsh, M. V. Kovalenko, *Nano Lett.* **2015**, 15, 3692.
- [16] J. A. Sichert, Y. Tong, N. Mutz, M. Vollmer, S. Fischer, K. Z. Milowska, R. García Cortadella, B. Nickel, C. Cardenas-Daw, J. K. Stolarczyk, A. S. Urban, J. Feldmann, *Nano Lett.* **2015**, 15, 6521.
- [17] D. H. Cao, C. C. Stoumpos, O. K. Farha, J. T. Hupp, M. G. Kanatzidis, *J. Am. Chem. Soc.* **2015**, 137, 7843.
- [18] E. R. Dohner, E. T. Hoke, H. I. Karunadasa, *J. Am. Chem. Soc.* **2014**, 136, 1718.
- [19] E. R. Dohner, A. Jaffe, L. R. Bradshaw, H. I. Karunadasa, *J. Am. Chem. Soc.* **2014**, 136, 13154.
- [20] M. Kulbak, D. Cahen, G. Hodes, *The Journal of Physical Chemistry Letters* **2015**, 6, 2452.
- [21] V. M. Goldschmidt, *Naturwissenschaften* **1926**, 14, 477.
- [22] C. Li, X. Lu, W. Ding, L. Feng, Y. Gao, Z. Guo, *Acta Crystallographica Section B* **2008**, 64, 702.
- [23] M. A. Green, A. Ho-Baillie, H. J. Snaith, *Nat Photon* **2014**, 8, 506.
- [24] D. B. Mitzi, *J. Chem. Soc., Dalton Trans.* **2001**, 1.
- [25] G. Kieslich, S. Sun, A. K. Cheetham, *Chemical Science* **2014**, 5, 4712.
- [26] M. Era, S. Morimoto, T. Tsutsui, S. Saito, *Appl. Phys. Lett.* **1994**, 65, 676.
- [27] X. Hong, T. Ishihara, A. V. Nurmikko, *Solid State Commun.* **1992**, 84, 657.
- [28] T. Hattori, T. Taira, M. Era, T. Tsutsui, S. Saito, *Chem. Phys. Lett.* **1996**, 254, 103.
- [29] T. Kondo, T. Azuma, T. Yuasa, R. Ito, *Solid State Commun.* **1998**, 105, 253.
- [30] K. Chondroudis, D. B. Mitzi, *Chem. Mater.* **1999**, 11, 3028.

- [31] F. Deschler, M. Price, S. Pathak, L. E. Klintberg, D. D. Jarausch, R. Higler, S. Hüttner, T. Leijskens, S. D. Stranks, H. J. Snaith, M. Atatüre, R. T. Phillips, R. H. Friend, *Journal of Physical Chemistry Letters* **2014**, 5, 1421.
- [32] N. Yantara, S. Bhaumik, F. Yan, D. Sabba, H. A. Dewi, N. Mathews, P. P. Boix, H. V. Demir, S. Mhaisalkar, *The Journal of Physical Chemistry Letters* **2015**, 6, 4360.
- [33] Y. Hassan, Y. Song, R. D. Pensack, A. I. Abdelrahman, Y. Kobayashi, M. A. Winnik, G. D. Scholes, *Adv. Mater.* **2015**, 28, 566.
- [34] L. C. Schmidt, A. Pertegás, S. González-Carrero, O. Malinkiewicz, S. Agouram, G. Mínguez Espallargas, H. J. Bolink, R. E. Galian, J. Pérez-Prieto, *J. Am. Chem. Soc.* **2014**, 136, 850.
- [35] D. Zhang, S. W. Eaton, Y. Yu, L. Dou, P. Yang, *J. Am. Chem. Soc.* **2015**, 137, 9230.
- [36] Q. Zhang, S. T. Ha, X. Liu, T. C. Sum, Q. Xiong, *Nano Lett.* **2014**, 14, 5995.
- [37] J. Burschka, N. Pellet, S.-J. Moon, R. Humphry-Baker, P. Gao, M. K. Nazeeruddin, M. Gratzel, *Nature* **2013**, 499, 316.
- [38] G. Li, Z. K. Tan, D. Di, M. L. Lai, L. Jiang, J. H. W. Lim, R. H. Friend, N. C. Greenham, *Nano Lett.* **2015**, 15, 2640.
- [39] J. Li, S. G. R. Bade, X. Shan, Z. Yu, *Adv. Mater.* **2015**, 27, 5196.
- [40] H. Cho, S.-H. Jeong, M.-H. Park, Y.-H. Kim, C. Wolf, C.-L. Lee, J. H. Heo, A. Sadhanala, N. Myoung, S. Yoo, S. H. Im, R. H. Friend, T.-W. Lee, *Science* **2015**, 350, 1222.
- [41] Y. C. Kim, N. J. Jeon, J. H. Noh, W. S. Yang, J. Seo, J. S. Yun, A. Ho-Baillie, S. Huang, M. A. Green, J. Seidel, T. K. Ahn, S. I. Seok, *Advanced Energy Materials* **2015**, 6, doi:10.1002/aenm.201502104.
- [42] G. E. Eperon, S. D. Stranks, C. Menelaou, M. B. Johnston, L. M. Herz, H. J. Snaith, *Energy and Environmental Science* **2014**, 7, 982.
- [43] C. C. Stoumpos, C. D. Malliakas, M. G. Kanatzidis, *Inorg. Chem.* **2013**, 52, 9019.
- [44] D. P. McMeekin, G. Sadoughi, W. Rehman, G. E. Eperon, M. Saliba, M. T. Hörantner, A. Haghighirad, N. Sakai, L. Korte, B. Rech, M. B. Johnston, L. M. Herz, H. J. Snaith, *Science* **2016**, 351, 151.
- [45] C. C. Stoumpos, C. D. Malliakas, J. A. Peters, Z. Liu, M. Sebastian, J. Im, T. C. Chasapis, A. C. Wibowo, D. Y. Chung, A. J. Freeman, B. W. Wessels, M. G. Kanatzidis, *Crystal Growth & Design* **2013**, 13, 2722.
- [46] S. Kondo, K. Takahashi, T. Nakanish, T. Saito, H. Asada, H. Nakagawa, *Current Applied Physics* **2007**, 7, 1.
- [47] Z. Cheng, J. Lin, *Crystengcomm* **2010**, 12, 2646.
- [48] L. Dou, A. B. Wong, Y. Yu, M. Lai, N. Kornienko, S. W. Eaton, A. Fu, C. G. Bischak, J. Ma, T. Ding, N. S. Ginsberg, L.-W. Wang, A. P. Alivisatos, P. Yang, *Science* **2015**, 349, 1518.
- [49] K. Gauthron, J. S. Lauret, L. Doyennette, G. Lanty, A. Al Choueiry, S. J. Zhang, A. Brehier, L. Largeau, O. Mauguin, J. Bloch, E. Deleporte, *Opt. Express* **2010**, 18, 5912.
- [50] A. Yanguis, D. Garrot, J. S. Lauret, A. Lusson, G. Bouchez, E. Deleporte, S. Pillet, E. E. Bendeif, M. Castro, S. Triki, Y. Abid, K. Boukheddaden, *Journal of Physical Chemistry C* **2015**, 119, 23638.
- [51] I. C. Smith, E. T. Hoke, D. Solis-Ibarra, M. D. McGehee, H. I. Karunadasa, *Angew. Chem.* **2014**, 126, 11414.
- [52] D. B. Mitzi, K. Chondroudis, C. R. Kagan, *Inorg. Chem.* **1999**, 38, 6246.
- [53] C. Motta, F. El-Mellouhi, S. Kais, N. Tabet, F. Alharbi, S. Sanvito, *Nat Commun* **2015**, 6.
- [54] T. Ishihara, J. Takahashi, T. Goto, *Physical Review B* **1990**, 42, 11099.
- [55] N. Kitazawa, M. Aono, Y. Watanabe, *J. Phys. Chem. Solids* **2011**, 72, 1467.
- [56] G. C. Papavassiliou, I. B. Koutselas, *Synth. Met.* **1995**, 71, 1713.

- [57] P. Tyagi, S. M. Arveson, W. A. Tisdale, *The Journal of Physical Chemistry Letters* **2015**, 6, 1911.
- [58] D. B. Mitzi, C. A. Feild, W. T. A. Harrison, A. M. Guloy, *Nature* **1994**, 369, 467.
- [59] J. Calabrese, N. L. Jones, R. L. Harlow, N. Herron, D. L. Thorn, Y. Wang, *J. Am. Chem. Soc.* **1991**, 113, 2328.
- [60] X. Wu, M. T. Trinh, D. Niesner, H. Zhu, Z. Norman, J. S. Owen, O. Yaffe, B. J. Kudisch, X. Y. Zhu, *J. Am. Chem. Soc.* **2015**, 137, 2089.
- [61] T. M. Koh, V. Shanmugam, J. Schlipf, L. M.-B. Oesinghaus, P., R. Narayanan, V. Swamy, N. Mathews, P. P. Boix, S. G. Mhaisalkar, *Adv. Mater.* **2016**, doi:10.1002/adma.201506141.
- [62] S. Zhang, G. Lanty, J.-S. Lauret, E. Deleporte, P. Audebert, L. Galmiche, *Acta Mater.* **2009**, 57, 3301.
- [63] S. Zhang, P. Audebert, Y. Wei, J.-S. Lauret, L. Galmiche, E. Deleporte, *J. Mater. Chem.* **2011**, 21, 466.
- [64] P. Audebert, G. Clavier, V. Alain-Rizzo, E. Deleporte, S. Zhang, J.-S. Lauret, G. Lanty, C. Boissière, *Chem. Mater.* **2009**, 21, 210.
- [65] M. Era, K. Maeda, T. Tsutsui, *Chem. Lett.* **1997**, 26, 1235.
- [66] M. I. Saidaminov, A. L. Abdelhady, B. Murali, E. Alarousu, V. M. Burlakov, W. Peng, I. Dursun, L. Wang, Y. He, G. MacUlan, A. Goriely, T. Wu, O. F. Mohammed, O. M. Bakr, *Nat. Commun.* **2015**, 6.
- [67] S. Gonzalez-Carrero, R. E. Galian, J. Perez-Prieto, *Journal of Materials Chemistry A* **2015**, 3, 9187.
- [68] H. Huang, A. S. Susha, S. V. Kershaw, T. F. Hung, A. L. Rogach, *Advanced Science* **2015**, 2, 1500194.
- [69] F. Zhang, H. Zhong, C. Chen, X. G. Wu, X. Hu, H. Huang, J. Han, B. Zou, Y. Dong, *ACS Nano* **2015**, 9, 4533.
- [70] A. B. Wong, M. Lai, S. W. Eaton, Y. Yu, E. Lin, L. Dou, A. Fu, P. Yang, *Nano Lett.* **2015**, 15, 5519.
- [71] J. Xing, X. F. Liu, Q. Zhang, S. T. Ha, Y. W. Yuan, C. Shen, T. C. Sum, Q. Xiong, *Nano Lett.* **2015**, 15, 4571.
- [72] X. Peng, L. Manna, W. Yang, J. Wickham, E. Scher, A. Kadavanich, A. P. Alivisatos, *Nature* **2000**, 404, 59.
- [73] S. Pathak, N. Sakai, F. Wisnivesky Rocca Rivarola, S. D. Stranks, J. Liu, G. E. Eperon, C. Ducati, K. Wojciechowski, J. T. Griffiths, A. A. Haghighirad, A. Pellaroque, R. H. Friend, H. J. Snaith, *Chem. Mater.* **2015**, 27, 8066.
- [74] A. Sadhanala, S. Ahmad, B. Zhao, N. Giesbrecht, P. M. Pearce, F. Deschler, R. L. Z. Hoyer, K. C. Gödel, T. Bein, P. Docampo, S. E. Dutton, M. F. L. De Volder, R. H. Friend, *Nano Lett.* **2015**, 15, 6095.
- [75] Q. A. Akkerman, V. D'Innocenzo, S. Accornero, A. Scarpellini, A. Petrozza, M. Prato, L. Manna, *J. Am. Chem. Soc.* **2015**, 137, 10276.
- [76] G. Nedelcu, L. Protesescu, S. Yakunin, M. I. Bodnarchuk, M. J. Grotevent, M. V. Kovalenko, *Nano Lett.* **2015**, 15, 5635.
- [77] A. Swarnkar, R. Chulliyil, V. K. Ravi, M. Irfanullah, A. Chowdhury, A. Nag, *Angew. Chem. Int. Ed.* **2015**, 54, 15424.
- [78] Y. Yin, A. P. Alivisatos, *Nature* **2005**, 437, 664.
- [79] B. Luo, Y.-C. Pu, Y. Yang, S. A. Lindley, G. Abdelmageed, H. Ashry, Y. Li, X. Li, J. Z. Zhang, *The Journal of Physical Chemistry C* **2015**, 119, 26672.
- [80] N. Pradhan, D. Reifsnnyder, R. Xie, J. Aldana, X. Peng, *J. Am. Chem. Soc.* **2007**, 129, 9500.
- [81] M. Zhang, H. Yu, M. Lyu, Q. Wang, J. H. Yun, L. Wang, *Chem. Commun.* **2014**, 50, 11727.

- [82] O. Vybornyi, S. Yakunin, M. V. Kovalenko, *Nanoscale* **2016**, doi:10.1039/C5NR06890H.
- [83] D. N. Dirin, S. Dreyfuss, M. I. Bodnarchuk, G. Nedelcu, P. Papagiorgis, G. Itskos, M. V. Kovalenko, *J. Am. Chem. Soc.* **2014**, 136, 6550.
- [84] Z. Ning, X. Gong, R. Comin, G. Walters, F. Fan, O. Voznyy, E. Yassitepe, A. Buin, S. Hoogland, E. H. Sargent, *Nature* **2015**, 523, 324.
- [85] R. S. Sanchez, M. S. de la Fuente, I. Suarez, G. Muñoz-Matutano, J. P. Martinez-Pastor, I. Mora-Sero, *Science Advances* **2016**, 2.
- [86] K. Wu, G. Liang, Q. Shang, Y. Ren, D. Kong, T. Lian, *J. Am. Chem. Soc.* **2015**, 137, 12792.
- [87] Y. Ling, Z. Yuan, Y. Tian, X. Wang, J. C. Wang, Y. Xin, K. Hanson, B. Ma, H. Gao, *Adv. Mater.* **2015**, 28, 305.
- [88] J. Even, L. Pedesseau, C. Katan, *ChemPhysChem* **2014**, 15, 3733.
- [89] Y. Bekenstein, B. A. Koscher, S. W. Eaton, P. Yang, A. P. Alivisatos, *J. Am. Chem. Soc.* **2015**, 137, 16008.
- [90] Z. Yuan, Y. Shu, Y. Tian, Y. Xin, B. Ma, *Chem. Commun.* **2015**, 51, 16385.
- [91] H. Deng, D. Dong, K. Qiao, L. Bu, B. Li, D. Yang, H. E. Wang, Y. Cheng, Z. Zhao, J. Tang, H. Song, *Nanoscale* **2015**, 7, 4163.
- [92] N. Kitazawa, Y. Watanabe, Y. Nakamura, *Journal of Materials Science* **2002**, 37, 3585.
- [93] D. M. Jang, K. Park, D. H. Kim, J. Park, F. Shojaei, H. S. Kang, J.-P. Ahn, J. W. Lee, J. K. Song, *Nano Lett.* **2015**, 15, 5191.
- [94] N. Pellet, J. Teuscher, J. Maier, M. Grätzel, *Chem. Mater.* **2015**, 27, 2181.
- [95] Z. Yuan, Y. Shu, Y. Xin, B. Ma, *Chem. Commun.* **2016**, 52, 3887.
- [96] J. B. Rivest, S. L. Swisher, L.-K. Fong, H. Zheng, A. P. Alivisatos, *ACS Nano* **2011**, 5, 3811.
- [97] D. H. Son, S. M. Hughes, Y. Yin, A. Paul Alivisatos, *Science* **2004**, 306, 1009.
- [98] L. Gil-Escrig, G. Longo, A. Pertegás, C. Roldán-Carmona, A. Soriano, M. Sessolo, H. J. Bolink, *Chem. Commun.* **2015**, 51, 569.
- [99] J. C. Yu, D. B. Kim, G. Baek, B. R. Lee, E. D. Jung, S. Lee, J. H. Chu, D. K. Lee, K. J. Choi, S. Cho, M. H. Song, *Adv. Mater.* **2015**, 27, 3492.
- [100] J. Wang, N. Wang, Y. Jin, J. Si, Z. K. Tan, H. Du, L. Cheng, X. Dai, S. Bai, H. He, Z. Ye, M. L. Lai, R. H. Friend, W. Huang, *Adv. Mater.* **2015**, 27, 2311.
- [101] R. L. Z. Hoyer, M. R. Chua, K. P. Musselman, G. Li, M. L. Lai, Z. K. Tan, N. C. Greenham, J. L. MacManus-Driscoll, R. H. Friend, D. Credgington, *Adv. Mater.* **2015**, 27, 1414.
- [102] Y. H. Kim, H. Cho, J. H. Heo, T. S. Kim, N. Myoung, C. L. Lee, S. H. Im, T. W. Lee, *Adv. Mater.* **2015**, 27, 1248.
- [103] X. Zhang, H. Lin, H. Huang, C. Reckmeier, Y. Zhang, W. C. H. Choy, A. L. Rogach, *Nano Lett.* **2016**, 16, 1415.
- [104] M. H. Song, J. C. Yu, D. B. Kim, E. D. Jung, B. R. Lee, *Nanoscale* **2016**, doi:10.1039/C5NR05604G
- [105] S. G. R. Bade, J. Li, X. Shan, Y. Ling, Y. Tian, T. Dilbeck, T. Besara, T. Geske, H. Gao, B. Ma, K. Hanson, T. Siegrist, C. Xu, Z. Yu, *ACS Nano* **2015**, 10, 1795.
- [106] H. Huang, F. Zhao, L. Liu, F. Zhang, X.-g. Wu, L. Shi, B. Zou, Q. Pei, H. Zhong, *ACS Applied Materials & Interfaces* **2015**, 7, 28128.
- [107] C. Eames, J. M. Frost, P. R. F. Barnes, B. C. O'Regan, A. Walsh, M. S. Islam, *Nat Commun* **2015**, 6.
- [108] T. Y. Yang, G. Gregori, N. Pellet, M. Grätzel, J. Maier, *Angewandte Chemie - International Edition* **2015**, 54, 7905.

- [109] H. Zhang, H. Lin, C. Liang, H. Liu, J. Liang, Y. Zhao, W. Zhang, M. Sun, W. Xiao, H. Li, S. Polizzi, D. Li, F. Zhang, Z. He, W. C. H. Choy, *Adv. Funct. Mater.* **2015**, 25, 7226.
- [110] V. D'Innocenzo, G. Grancini, M. J. P. Alcocer, A. R. S. Kandada, S. D. Stranks, M. M. Lee, G. Lanzani, H. J. Snaith, A. Petrozza, *Nature communications* **2014**, 5, 3586.
- [111] J. S. Manser, P. V. Kamat, *Nat Photon* **2014**, 8, 737.
- [112] Q. Dong, Y. Fang, Y. Shao, P. Mulligan, J. Qiu, L. Cao, J. Huang, *Science* **2015**, 347, 967.
- [113] D. Shi, V. Adinolfi, R. Comin, M. Yuan, E. Alarousu, A. Buin, Y. Chen, S. Hoogland, A. Rothenberger, K. Katsiev, Y. Losovyj, X. Zhang, P. A. Dowben, O. F. Mohammed, E. H. Sargent, O. M. Bakr, *Science* **2015**, 347, 519.
- [114] S. D. Stranks, H. J. Snaith, *Nat. Nanotechnol.* **2015**, 10, 391.
- [115] C. Wehrenfennig, G. E. Eperon, M. B. Johnston, H. J. Snaith, L. M. Herz, *Adv. Mater.* **2014**, 26, 1584.
- [116] J. M. Azpiroz, E. Mosconi, J. Bisquert, F. De Angelis, *Energy Environ. Sci.* **2015**, 8, 2118.
- [117] M. Lenes, G. Garcia-Belmonte, D. Tordera, A. Pertegás, J. Bisquert, H. J. Bolink, *Advanced Functional Materials* **2011**, 21, 1581.
- [118] M. F. Aygüler, M. D. Weber, B. M. D. Puscher, D. D. Medina, P. Docampo, R. D. Costa, *The Journal of Physical Chemistry C* **2015**, 119, 12047.
- [119] M. Saba, M. Cadelano, D. Marongiu, F. Chen, V. Sarritzu, N. Sestu, C. Figus, M. Aresti, R. Piras, A. Geddo, Lehmann, C. Cannas, A. Musinu, F. Quochi, A. Mura, G. Bongiovanni, *Nat Commun* **2014**, 5.
- [120] S. D. Stranks, S. M. Wood, K. Wojciechowski, F. Deschler, M. Saliba, H. Khandelwal, J. B. Patel, S. J. Elston, L. M. Herz, M. B. Johnston, A. P. H. J. Schenning, M. G. Debije, M. K. Riede, S. M. Morris, H. J. Snaith, *Nano Lett* **2015**, 15, 4935.
- [121] M. Saliba, S. M. Wood, J. B. Patel, P. K. Nayak, J. Huang, J. A. Alexander-Webber, B. Wenger, S. D. Stranks, M. T. Hörantner, J. T.-W. Wang, R. J. Nicholas, L. M. Herz, M. B. Johnston, S. M. Morris, H. J. Snaith, M. K. Riede, *Adv. Mater.* **2015**, 28, 923.
- [122] Q. Liao, K. Hu, H. H. Zhang, X. D. Wang, J. N. Yao, H. B. Fu, *Adv Mater* **2015**, 27, 3405.
- [123] M. H. Huang, S. Mao, H. Feick, H. Q. Yan, Y. Y. Wu, H. Kind, E. Weber, R. Russo, P. D. Yang, *Science* **2001**, 292, 1897.
- [124] H. M. Zhu, Y. P. Fu, F. Meng, X. X. Wu, Z. Z. Gong, Q. Ding, M. V. Gustafsson, M. T. Trinh, S. Jin, X. Y. Zhu, *Nat Mater* **2015**, 14, 636.
- [125] V. I. Klimov, S. A. Ivanov, J. Nanda, M. Achermann, I. Bezel, J. A. McGuire, A. Piryatinski, *Nature* **2007**, 447, 441.
- [126] V. I. Klimov, A. A. Mikhailovsky, S. Xu, A. Malko, J. A. Hollingsworth, C. A. Leatherdale, H. J. Eisler, M. G. Bawendi, *Science* **2000**, 290, 314.
- [127] Y. Wang, X. Li, J. Song, L. Xiao, H. Zeng, H. Sun, *Adv. Mater.* **2015**, 27, 7101.
- [128] J. Pan, S. P. Sarmah, B. Murali, I. Dursun, W. Peng, M. R. Parida, J. Liu, L. Sinatra, N. Alyami, C. Zhao, E. Alarousu, T. K. Ng, B. S. Ooi, O. M. Bakr, O. F. Mohammed, *The Journal of Physical Chemistry Letters* **2015**, 6, 5027.
- [129] S. Yakunin, L. Protesescu, F. Krieg, M. I. Bodnarchuk, G. Nedelcu, M. Humer, G. De Luca, M. Fiebig, W. Heiss, M. V. Kovalenko, *Nat Commun* **2015**, 6.
- [130] T. C. Sum, S. Chen, G. Xing, X. Liu, B. Wu, *Nanotechnology* **2015**, 26, 342001.
- [131] T. J. Savenije, C. S. Ponseca, L. Kunneman, M. Abdellah, K. B. Zheng, Y. X. Tian, Q. S. Zhu, S. E. Canton, I. G. Scheblykin, T. Pullerits, A. Yartsev, V. Sundstrom, *J. Phys. Chem. Lett.* **2014**, 5, 2189.
- [132] X. Dai, Z. Zhang, Y. Jin, Y. Niu, H. Cao, X. Liang, L. Chen, J. Wang, X. Peng, *Nature* **2014**, 515, 96.
- [133] J. Song, J. Li, X. Li, L. Xu, Y. Dong, H. Zeng, *Adv. Mater.* **2015**, 27, 7162.

- [134] Y. Kim, E. Yassitepe, O. Voznyy, R. Comin, G. Walters, X. Gong, P. Kanjanaboos, A. F. Nogueira, E. H. Sargent, *ACS Applied Materials & Interfaces* **2015**, 7, 25007.
- [135] T. M. Brenner, D. A. Egger, A. M. Rappe, L. Kronik, G. Hodes, D. Cahen, *The Journal of Physical Chemistry Letters* **2015**, 6, 4754.
- [136] W. Nie, H. Tsai, R. Asadpour, J.-C. Blancon, A. J. Neukirch, G. Gupta, J. J. Crochet, M. Chhowalla, S. Tretiak, M. A. Alam, H.-L. Wang, A. D. Mohite, *Science* **2015**, 347, 522.
- [137] H. Zhou, Y. Shi, Q. Dong, H. Zhang, Y. Xing, K. Wang, Y. Du, T. Ma, *The Journal of Physical Chemistry Letters* **2014**, 5, 3241.
- [138] M. H. Kumar, S. Dharani, W. L. Leong, P. P. Boix, R. R. Prabhakar, T. Baikie, C. Shi, H. Ding, R. Ramesh, M. Asta, M. Graetzel, S. G. Mhaisalkar, N. Mathews, *Adv. Mater.* **2014**, 26, 7122.
- [139] B.-W. Park, B. Philippe, X. Zhang, H. Rensmo, G. Boschloo, E. M. J. Johansson, *Adv. Mater.* **2015**, 27, 6806.
- [140] M. Cadelano, V. Sarritzu, N. Sestu, D. Marongiu, F. Chen, R. Piras, R. Corpino, C. M. Carbonaro, F. Quochi, M. Saba, A. Mura, G. Bongiovanni, *Advanced Optical Materials* **2015**, 3, 1557.
- [141] M. Li, G. Xing, G. Xing, B. Wu, T. Wu, X. Zhang, T. C. Sum, *Physical Review B* **2013**, 87, 115309.
- [142] M. Panahandeh-Fard, J. Yin, M. Kurniawan, Z. Wang, G. Leung, T. C. Sum, C. Soci, *The Journal of Physical Chemistry Letters* **2014**, 5, 1144.
- [143] G. Christmann, R. Butté, E. Feltin, J.-F. Carlin, N. Grandjean, *Appl. Phys. Lett.* **2008**, 93, 051102.
- [144] G. Lanty, J. S. Lauret, E. Deleporte, S. Bouchoule, X. Lafosse, *Appl. Phys. Lett.* **2008**, 93, 081101.
- [145] G. Lanty, S. Zhang, J. S. Lauret, E. Deleporte, P. Audebert, S. Bouchoule, X. Lafosse, J. Zuñiga-Pérez, F. Semon, D. Lagarde, F. Médard, J. Leymarie, *Physical Review B* **2011**, 84, 195449.
- [146] E. B. Namdas, M. Tong, P. Ledochowitsch, S. R. Mednick, J. D. Yuen, D. Moses, A. J. Heeger, *Adv. Mater.* **2009**, 21, 799.
- [147] T. Takenobu, S. Z. Bisri, T. Takahashi, M. Yahiro, C. Adachi, Y. Iwasa, *Phys Rev Lett* **2008**, 100, 066601.
- [148] R. Meerheim, M. Furno, S. Hofmann, B. Lüssem, K. Leo, *Applied Physics Letters* **2010**, 97, 253305.
- [149] N. K. Kumawat, A. Dey, K. L. Narasimhan, D. Kabra, *ACS Photonics* **2015**, 2, 349.
- [150] J. C. Yu, D. B. Kim, E. D. Jung, B. R. Lee, M. H. Song, *Nanoscale* **2016**, doi:10.1039/C5NR05604G
- [151] B. R. Sutherland, S. Hoogland, M. M. Adachi, C. T. O. Wong, E. H. Sargent, *Acs Nano* **2014**, 8, 10947.
- [152] R. Dhankar, A. N. Brigeman, A. V. Larsen, R. J. Stewart, J. B. Asbury, N. C. Giebink, *Appl Phys Lett* **2014**, 105.
- [153] S. W. Eaton, M. Lai, N. A. Gibson, A. B. Wong, L. Dou, J. Ma, L.-W. Wang, S. R. Leone, P. Yang, *Proceedings of the National Academy of Sciences* **2016**, 113, 1993.

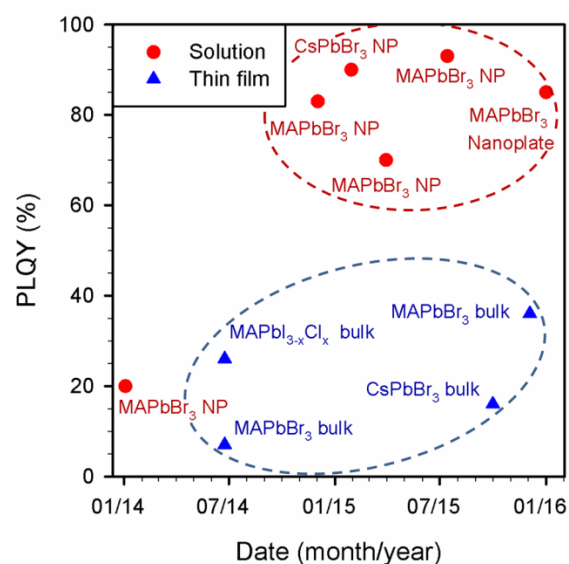


Figure 1. Evolution of PLQY value of perovskite materials in bulk and nanoparticle (NP) form.

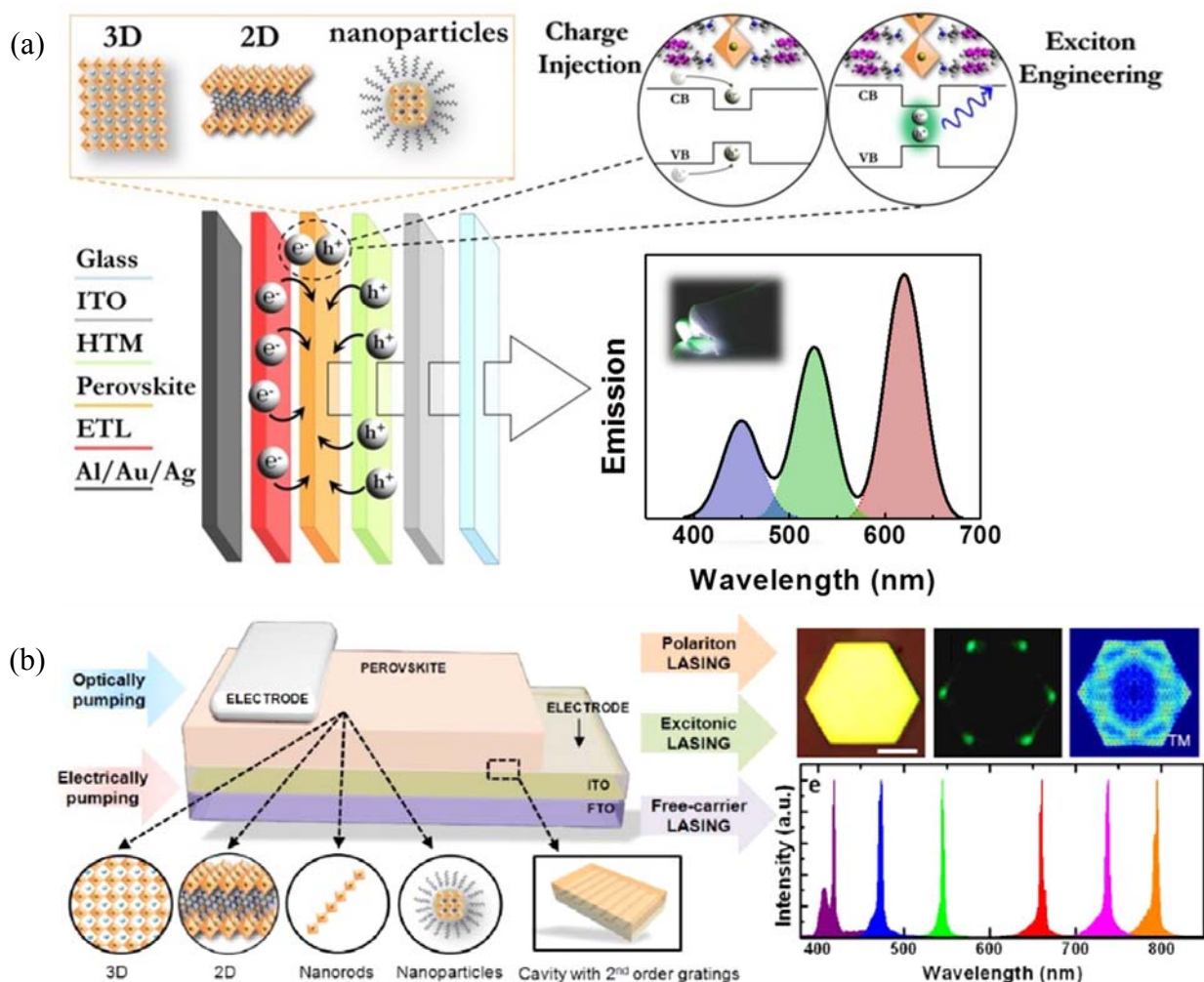


Figure 2. Schematic representation of a (a) PeLED device concept and (b) perovskite laser device concept.

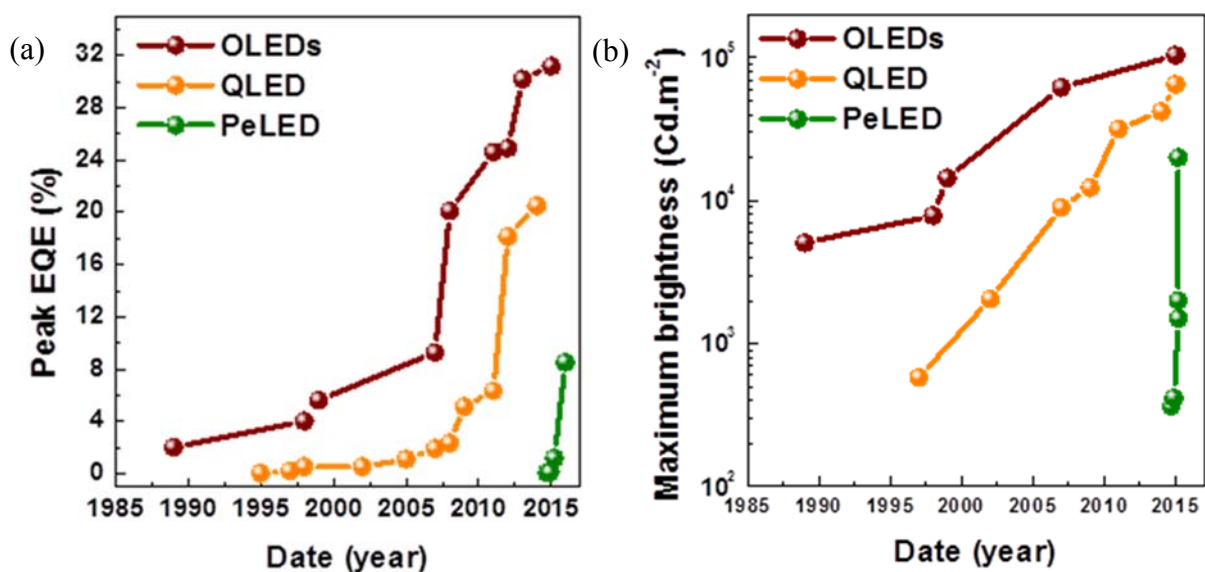


Figure 3. Evolution of representative (a) EQE and (b) maximum brightness for perovskite, quantum dot and organic light emission diodes.

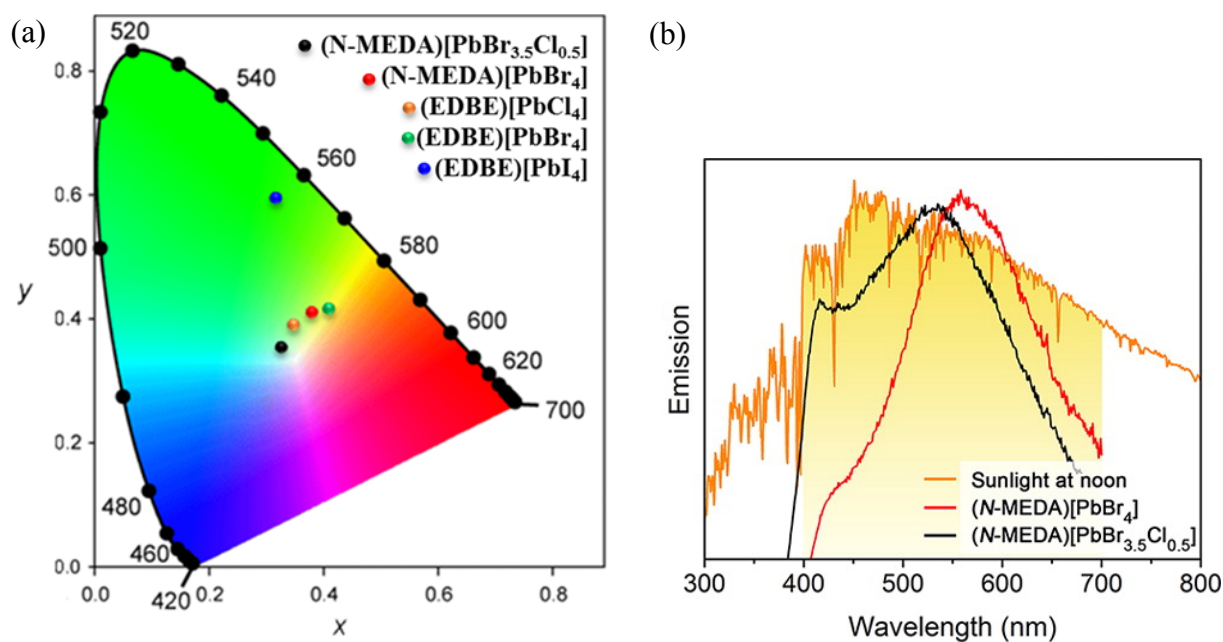


Figure 4. (a) PL emission position of various layered perovskites on the CIE diagram. Adapted with permission from Refs.^[18, 19]. Copyright 2014 American Chemical Society. (b) Example of white light emission spectra from an individual perovskite emitter. Reproduced with permission from Ref. ^[18]. Copyright 2014 American Chemical Society.

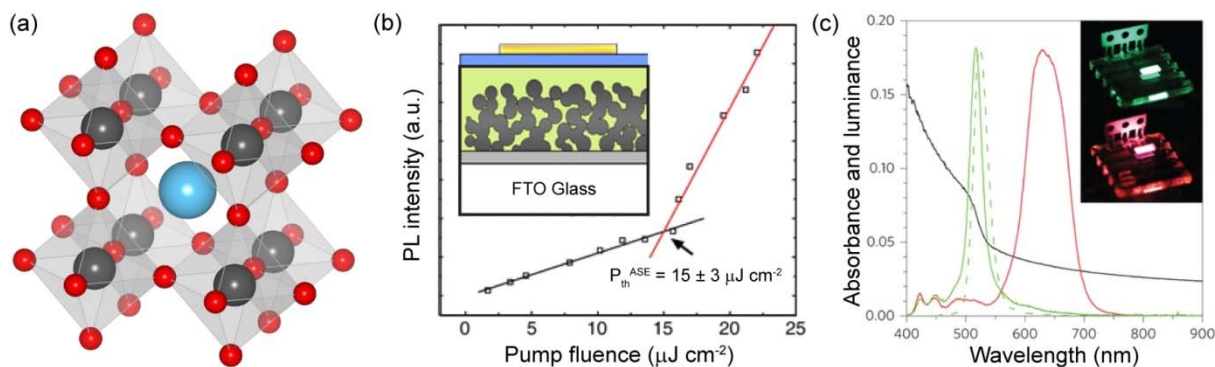


Figure 5. (a) Schematic representation of the perovskite crystal structure. Blue, grey, and red spheres represent the A-, M-, and X-site atoms, respectively. (b) PL intensity as a function of pump fluence showing ASE threshold of the solar cell configuration with mesoporous TiO_2 scaffold (inset). Reproduced with permission from Ref. [2]. Copyright 2014, Nature Publishing Group. (c) Optical absorption spectrum (black), normalized electroluminescence and photoluminescence (green; solid and dashed line, respectively) spectra of $\text{CH}_3\text{NH}_3\text{PbBr}_3$ perovskite. Electroluminescence spectrum of $\text{CH}_3\text{NH}_3\text{PbBr}_2\text{I}$ mixed halide perovskite is shown in red. Inset: green and red electroluminescence from $\text{CH}_3\text{NH}_3\text{PbBr}_3$ and $\text{CH}_3\text{NH}_3\text{PbBr}_2\text{I}$ -based PeLEDs, respectively. Reproduced with permission from Ref. [5]. Copyright 2014, Nature Publishing Group.

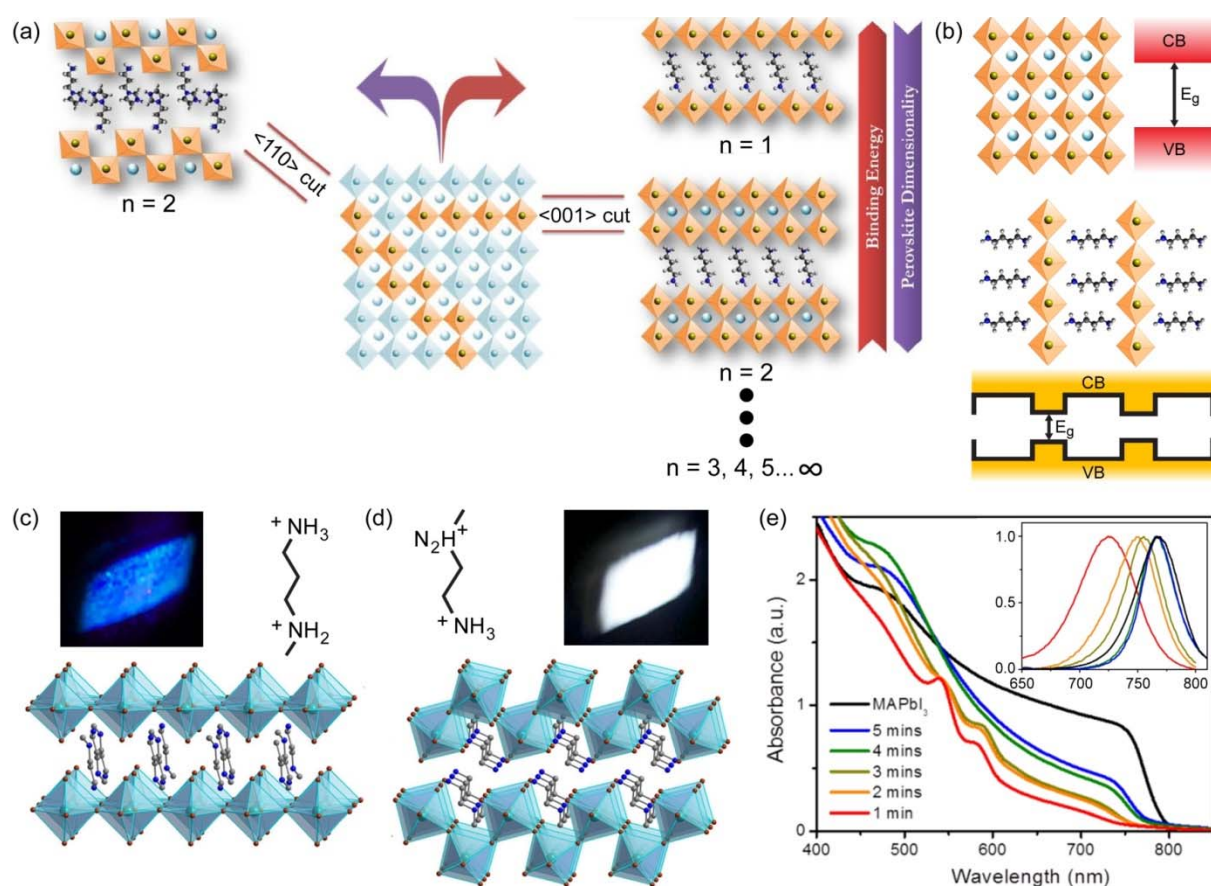


Figure 6. (a) Concept of multi-dimensionality in perovskite materials; introduction of large organic cations in the inorganic layers break the AMX_3 symmetry to form perovskites in $\langle 110 \rangle$ and $\langle 001 \rangle$ oriented A_2MX_4 layered structures. (b) Schematic representation of the band gap between valence and conduction band (VB and CB, respectively) in a 3D perovskite (top) and the band gap in 2D layered perovskite (bottom). Layered perovskites form a natural quantum well, in which the inorganic sheets and organic molecules act as ‘well’ and ‘barrier’, respectively. Intercalation of (c) N^1 -methylpropane-1,3-diammonium (N -MPDA) and (d) N^1 -methylethane-1,2-diammonium (N -MEDA), within the inorganic $PbBr_4^{2-}$ sheets resulted in a blue-emitting $\langle 001 \rangle$ and white-light emitting $\langle 110 \rangle$ oriented structures, respectively. Turquoise, brown, blue, and gray spheres represent Pb, Br, N, and C atoms, respectively. Green spheres represent $CH_3NH_3^+$. (c-d) Adapted with permission from Ref. [18]. Copyright 2014 American Chemical Society. (e) Optical absorption spectra of $CH_3NH_3PbI_3$ (black) and $(IC_2H_4NH_3)_2(CH_3NH_3)_{n-1}PbnI_{3n+1}$ perovskite films at different dipping times. Inset: corresponding PL spectra. Reproduced with permission from Ref. [61]. Copyright 2015, Wiley-VCH.

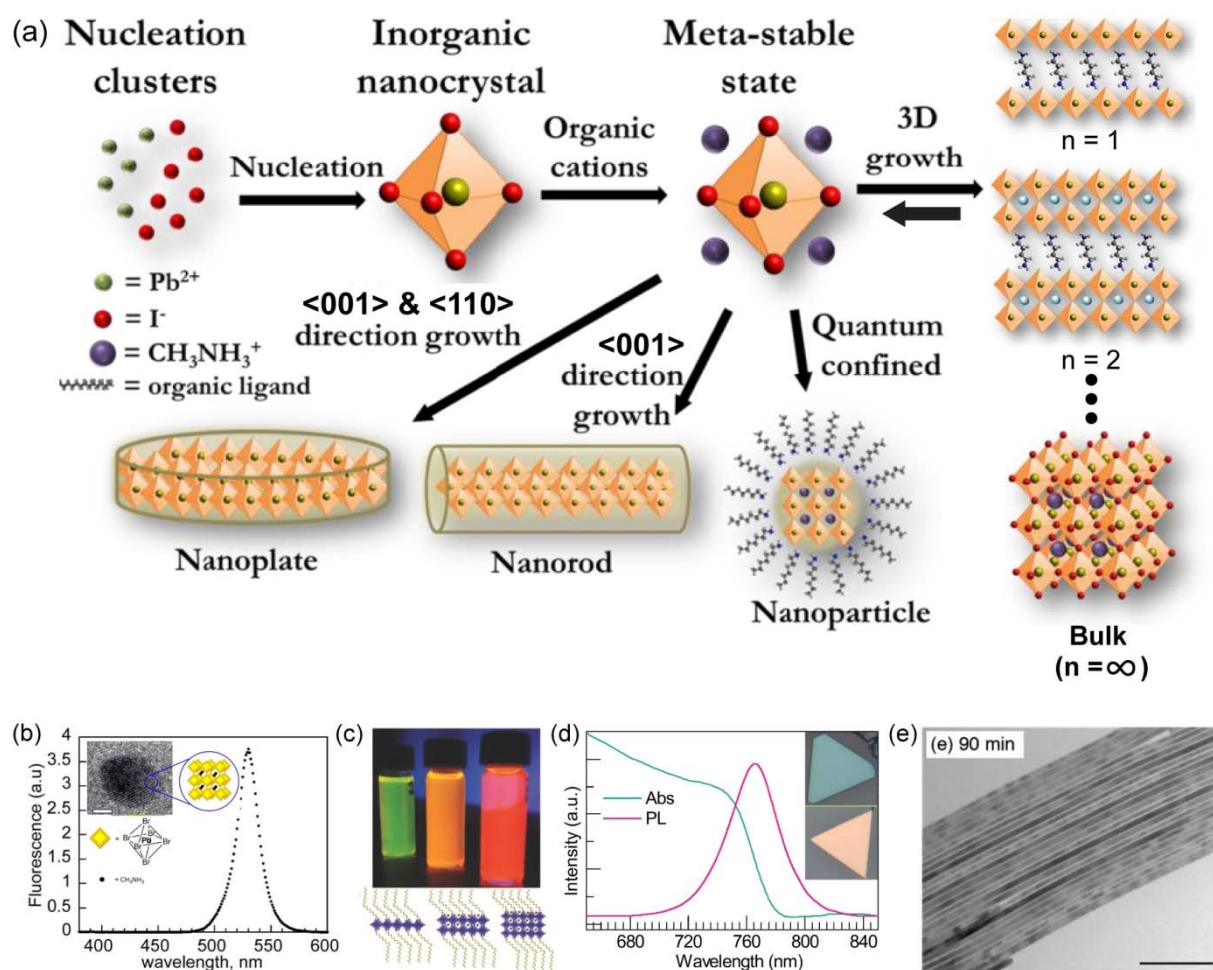


Figure 7. (a) Schematic representation of the hybrid perovskite phase formation and the resulting morphologies. (b) Green photoluminescence of 6 nm-sized $\text{CH}_3\text{NH}_3\text{PbBr}_3$ NPs. Inset: HRTEM image of individual nanoparticle (scale bar 2 nm). Adapted with permission from Ref. [34]. Copyright 2014 American Chemical Society. (c) Top: Photograph of colloidal 2D organo-lead iodide perovskite NC solutions under ambient light of (from left to right) $n = 1, 2$, and 3 , respectively. Bottom: schematic structures of the colloidal 2D organo-lead iodide perovskites NPs ($\text{C}_{18}\text{H}_{35}\text{NH}_3)_2(\text{CH}_3\text{NH}_3)_{n-1}[\text{Pb}_n\text{I}_{3n+1}]$, where (from left to right) $n = 1, 2$, and 3 . Reproduced with permission from Ref. [33]. Copyright 2015, Wiley-VCH. (d) Absorbance and photoluminescence spectra of chemical-vapor deposited $\text{CH}_3\text{NH}_3\text{PbI}_3$ NPLs on a mica substrate. Inset: Optical images of NPLs; the optical contrast corresponds to different NPL thickness. Adapted with permission from Ref. [36]. Copyright 2014 American Chemical Society. (e) CsPbBr_3 NWs formed through the self-assembly of nanocubes after 90 min of reaction. Adapted with permission from Ref. [35]. Copyright 2015 American Chemical Society.

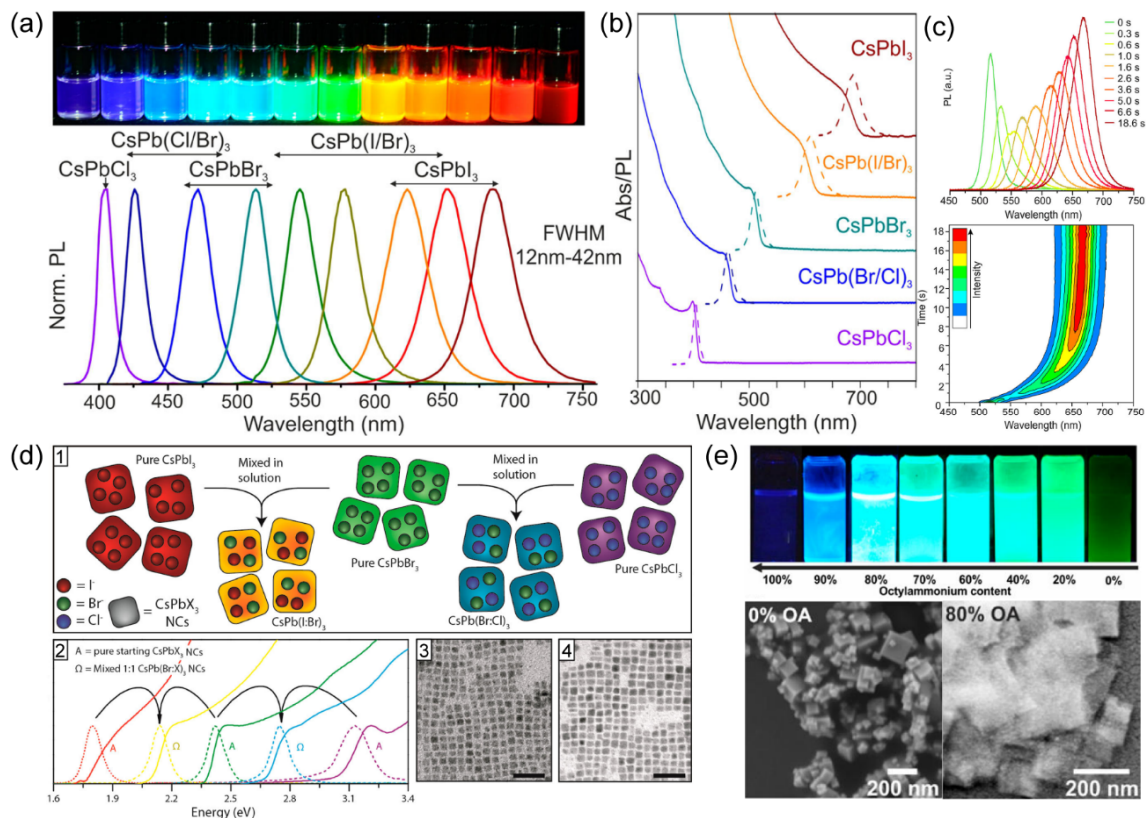


Figure 8. (a) Colloidal CsPbX_3 ($X = \text{Cl}^-$, Br^- , and I^-) perovskite NPs solutions with tunable band gap energies covering the entire visible spectrum. Top: colloidal NPs solutions in toluene under UV lamp illumination ($\lambda = 365$ nm). Bottom: representative PL spectra; (b) Typical PL and optical absorption spectra of colloidal solutions from Figure (a); Figure (a-b) reprinted with permission from Ref. [15]. Copyright 2015 American Chemical Society. (c) In-situ PL measurement of CsPbBr_3 to CsPbI_3 conversion at 40 °C using $[\text{Br}]_{\text{parent}}/[\text{I}]_{\text{incoming}} = 1:3$; Figure (c) reprinted with permission from Ref. [76]. Copyright 2015 American Chemical Society. (d) Schematic representation of inter-particle anion exchange (Panel 1). Panel 2: optical absorption and PL spectra of various $\text{CsPb}(\text{Cl/Br})_3$ and $\text{CsPb}(\text{Br/I})_3$ NPs prepared via inter-particle anion exchange. Panel 3-4: TEM images of mixed $\text{CsPbBr}_3:\text{CsPbCl}_3$ (1:1) and $\text{CsPbBr}_3:\text{CsPbI}_3$ (1:1) NPs, respectively. Scale bars correspond to 50 nm. Reprinted with permission from Ref. [75]. Copyright 2015 American Chemical Society. (e) Photographs of colloidal solutions in toluene with varying octylammonium content under UV lamp (top) and TEM images of NPLs and NPs prepared with 80% and 0% octylammonium, respectively (bottom). Reprinted with permission from Ref. [16]. Copyright 2015 American Chemical Society.

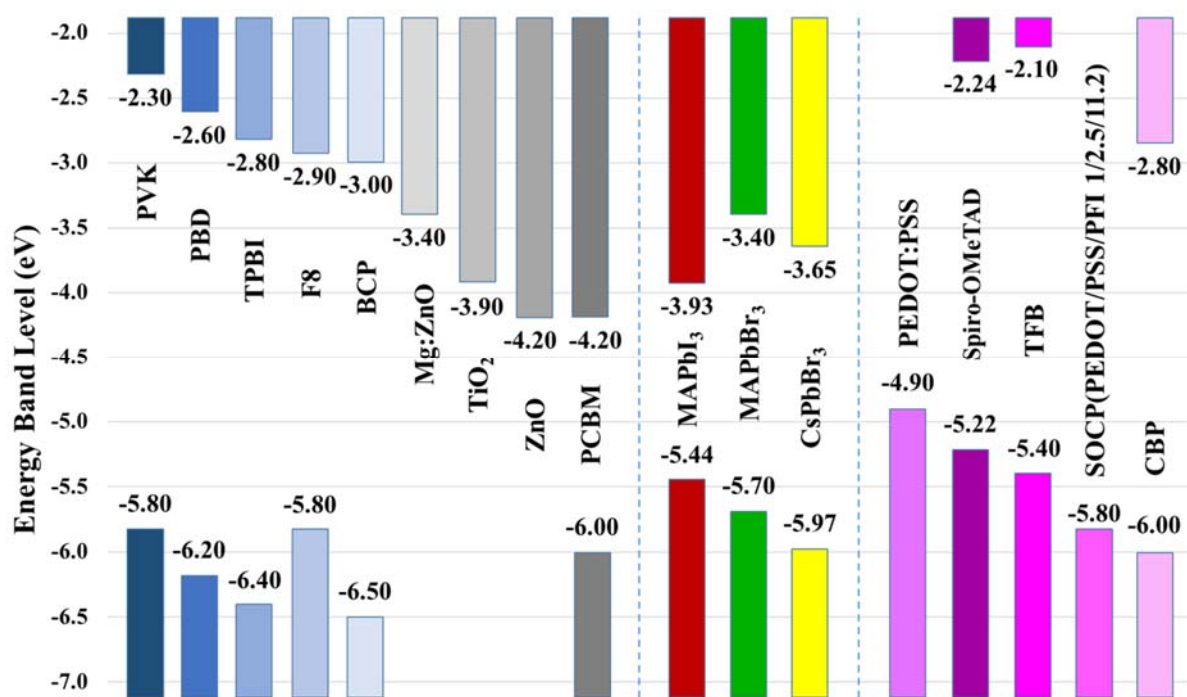


Figure 9. Energy levels for different materials acting as electron transporting layer (left), thin film 3D perovskite emitter (middle) and hole transporting layer (right) in PeLEDs.

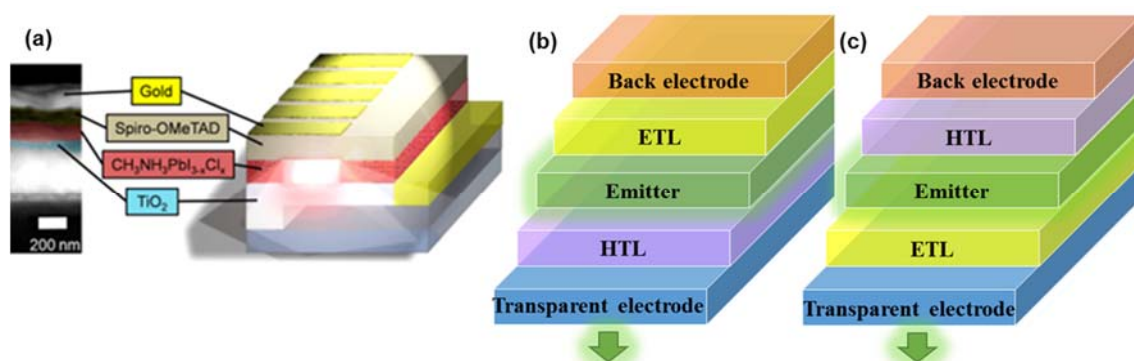


Figure 10. (a) Schematic diagram and cross sectional images of PeLED adapted from solar cell configuration using mesoporous TiO₂ and spiro-MeOTAD as ETL and HTL respectively. Reprinted with permission from Ref. ^[4]. Copyright 2015 American Chemical Society. Schematic representation of PeLED architecture with HTL/perovskite/ETL (b) and ETL/perovskite/HTL (c) configuration.

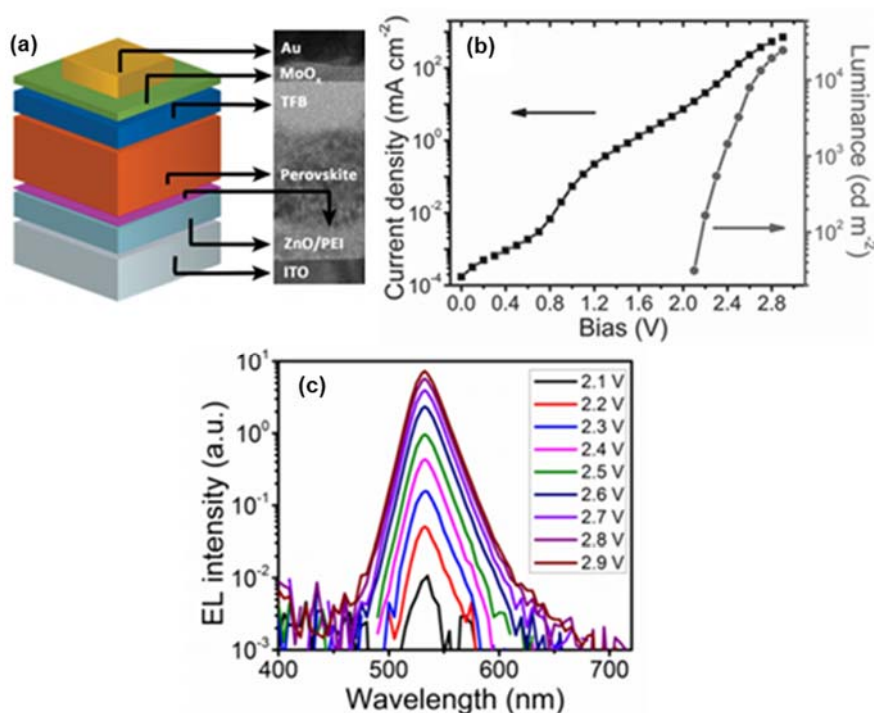


Figure 11. (a) Cross-sectional microscopy image and schematic PeLED diagram, in which poly(ethylenimine) interlayer is deposited between the ETL and perovskite emitter layer. (b) The voltage vs current density and luminance curve of a state-of-the-art $\text{CH}_3\text{NH}_3\text{PbBr}_3$ -based LED with ETL/perovskite/HTL device structure. (c) The electroluminescence spectra at various applied voltages indicate that the emission originates from the $\text{CH}_3\text{NH}_3\text{PbBr}_3$ layer alone. Figures (a-c) are reproduced with permission from Ref. [100]. Copyright 2015, Wiley-VCH.

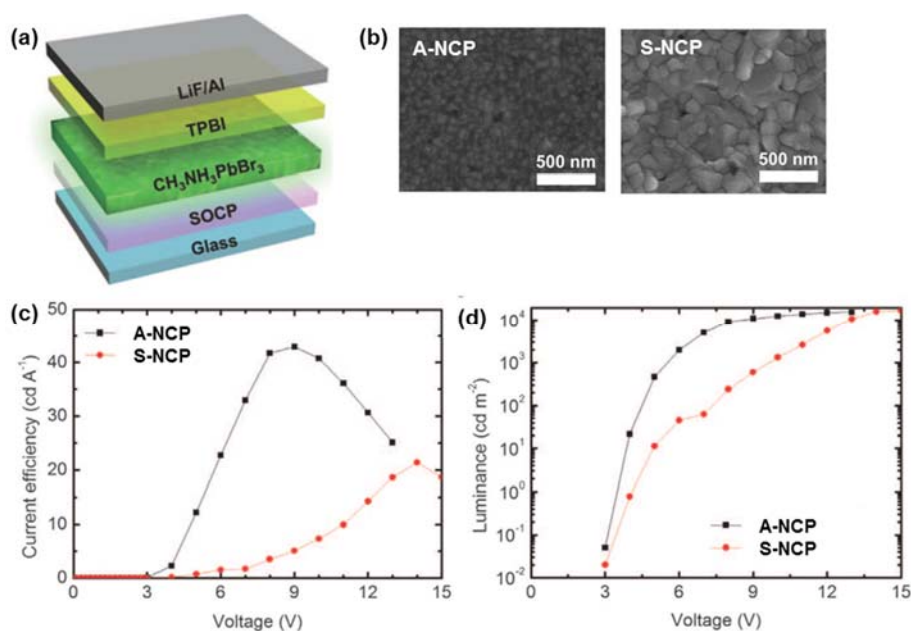


Figure 12. (a) Schematic device diagram of PeLED architecture adopted to reveal importance of emitter grain size on PeLED performance. (b) Scanning electron microscopy image of the $\text{CH}_3\text{NH}_3\text{PbBr}_3$ emitter top morphology grown using various nanocrystal pinning (NCP) techniques to modulate grain size. Corresponding (c) current efficiency versus voltage and (d)

luminance versus voltage curves of PeLED exposed the importance of reducing the emitter grain size. Figures (a-d) are reprinted with permission from Ref. [40]. Copyright 2015, AAAS.

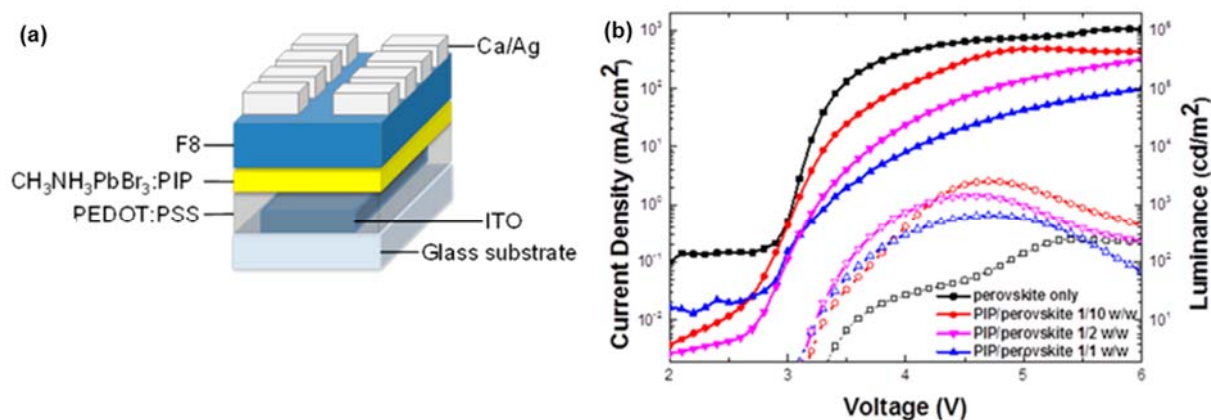


Figure 13. Schematic diagram of PeLED configuration with $\text{CH}_3\text{NH}_3\text{PbBr}_3$:PIP blend as emitter layer (a). The voltage versus current density (solid lines) and luminance (dashed line) (b) curve of PeLED at various PIP concentrations indicating the active role the PIP polymer plays to passivate pin holes and reduce non-radiative shunt resistances. Reprinted with permission from Ref. [38]. Copyright 2015, American Chemical Society.

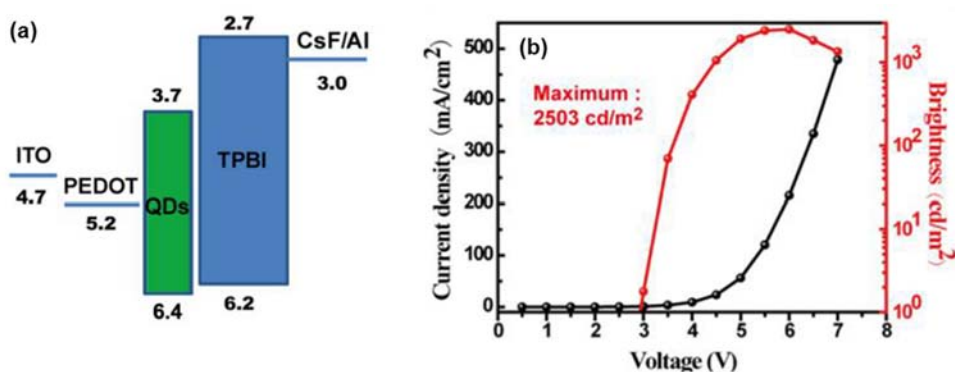


Figure 14. (a) Band alignment diagram of PeLED with $\text{CH}_3\text{NH}_3\text{PbBr}_3$ quantum dots as emissive layer. (b) Voltage vs current density and luminance curves. Reprinted with permission from Ref. [106]. Copyright 2015, American Chemical Society.

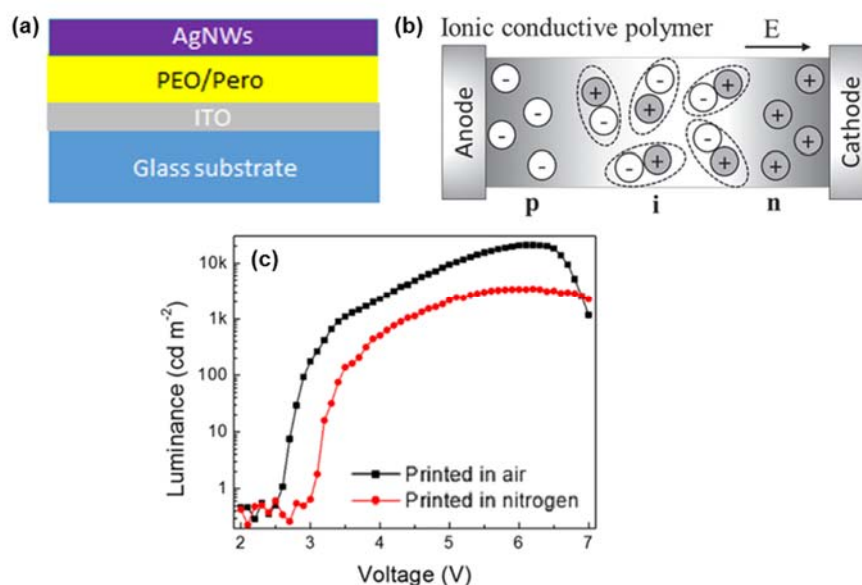


Figure 15. (a) PeLED architecture employing a perovskite:PEO blend as emitter layer sandwiched between two electrodes. Reproduced with permission from Ref. ^[105]. Copyright 2015, American Chemical Society. (b) Schematic illustration of ion migration occurring within the emitter layer under applied bias, which results in self-doping and consequently in p-i-n formation. Reproduced with permission from Ref. ^[39]. Copyright 2015, Wiley-VCH. (c) The luminance versus voltage (c) curve of PeLEDs with the perovskite/PEO layer printed in air (square) and in nitrogen (circle) environment is also presented, highlighting the stability towards moisture and air. Reproduced with permission from Ref. ^[105]. Copyright 2015, American Chemical Society.

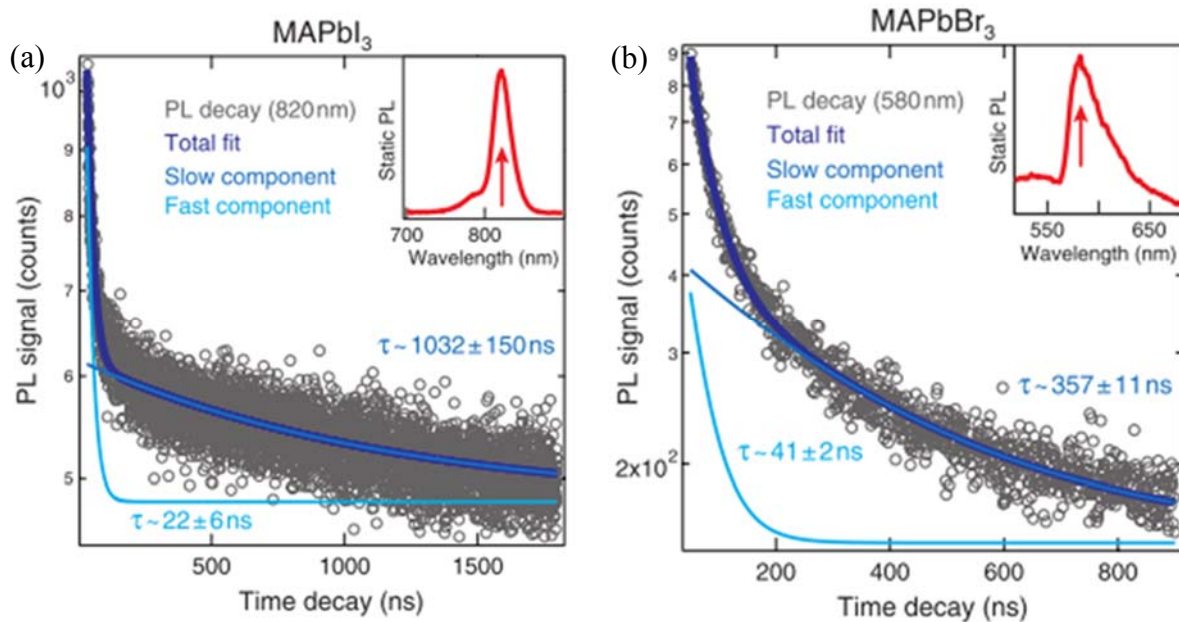


Figure 16. (a) and (b) $\text{CH}_3\text{NH}_3\text{PbI}_3$ and $\text{CH}_3\text{NH}_3\text{PbBr}_3$ PL decays corresponding to diffusion lengths of $\sim 8 \mu\text{m}$ and $\sim 3 \mu\text{m}$ respectively. Reproduced with permission from Ref. ^[113]. Copyright 2015, AAAS.

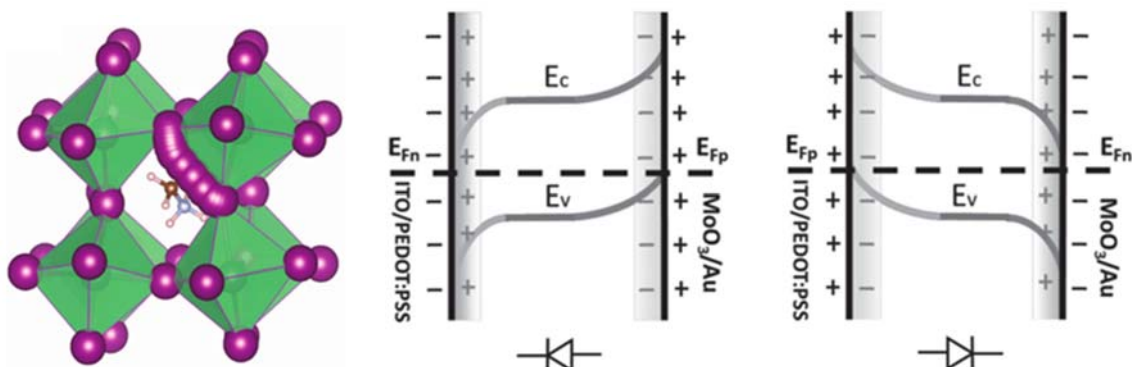


Figure 17. (a) Schematic representation of the possible mechanism of ionic (halide) motion. Reprinted with permission from Ref. ^[107]. (b) Band diagram of a perovskite LEC device acting as forward diode because of positive charge is accumulated near the ITO/PEDOT:PSS electrode and (c) Vice versa. Interface charge and screen charge are represented in grey and black, respectively. Figure (b-c) reproduced with permission from Ref. ^[109]. Copyright 2015, Wiley-VCH.

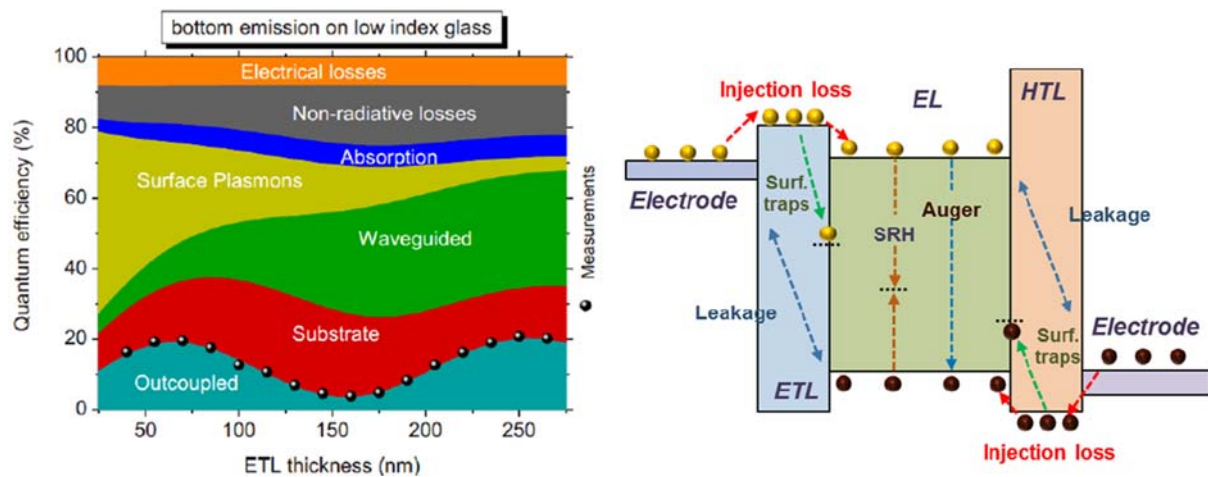


Figure 18. (a) Estimation of the losses in an organic light emitting diode as a function of the ETL thickness. Reproduced with permission from Ref. ^[148]. Copyright 2010, AIP Publishing LLC. **(b)** Schematic representation of the processes responsible of the electrical losses in a light emitting diode.

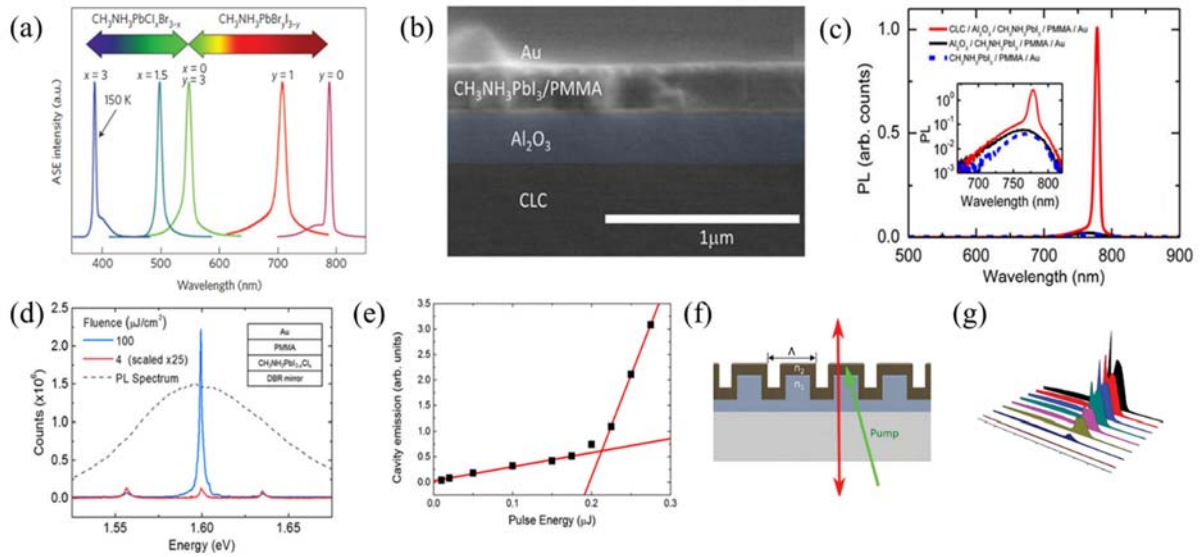


Figure 19. ASE/lasing based on organic-inorganic 3D perovskites films. **(a)** Wide wavelength tunability of ASE from low-temperature solution-processed organic-inorganic halide perovskite films fabricated by mixing the precursor solutions. (a) Reproduced with permission from Ref. [2]. Copyright 2014, Nature Publishing Group. **(b)** SEM cross-section image of the multilayers structure on glass for the lower threshold ASE. The alumina layer has been shaded for contrast. **(c)** Emission from full device stack (red), stack without CLC (black), and stack without CLC and alumina (blue dashed), with pulsed excitation (530 nm, 4-ns pulses, $\sim 60 \mu\text{J}/\text{cm}^2$). (b-c) Reproduced with permission from Ref. [120]. Copyright 2015, American Chemical Society. **(d)** RT PL spectra of a vertical microcavity with the structure as shown in the inset using a perovskite film as the gain medium excited with 400 ps pulsed laser at 2.33 eV. **(e)** Pump fluence dependent PL intensity of the 1.6 eV mode shows a lasing threshold at around 0.2 μJ per pulse. (d-e) Reproduced with permission from Ref. [31]. Copyright 2015, American Chemical Society. **(f)** Illustration of a DFB cavity with a perovskite/patterned polymer resist/glass structure. **(g)** PL spectra from a perovskite DFB laser with 400 nm periodicity upon photoexcitation with 532 nm light with 1 ns pulses at fluences from 0.04 to 4.35 $\mu\text{J}/\text{cm}^2$. (f-g) Reproduced with permission from Ref. [121]. Copyright 2015, Wiley-VCH.

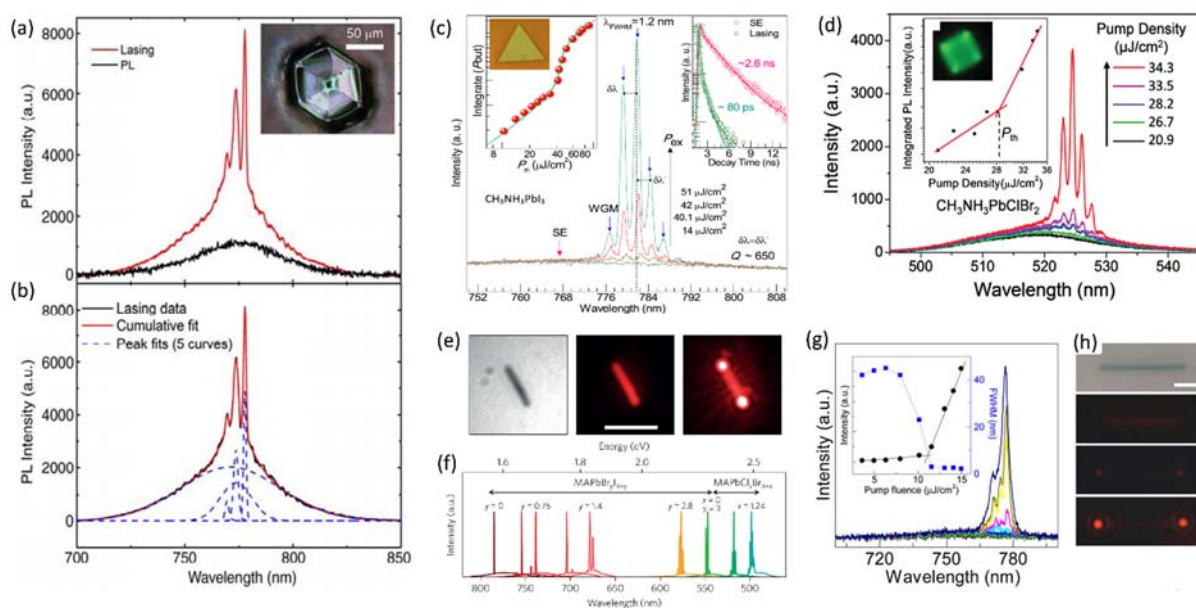


Figure 20. RT lasing from organic-inorganic perovskite micro/nanocavity. **(a)** Lasing spectra from CH₃NH₃PbI₃ single crystals from dropcasted films. Inset shows the photograph of the crystal. **(b)** Fitted lasing spectra with five peaks, in which the most prominent mode shows a full width half maximum of 1.2 nm. (a,b) Reproduced with permission from Ref. [2]. Copyright 2014, Nature Publishing Group. **(c)** The evolution from spontaneous emission to WGM lasing in a vapor-phase-grown CH₃NH₃PbI₃ triangular microplatelet (optical image inset; thickness, 150 nm; edge length, 32 μm). Left inset: integrated PL intensities as a function of pump fluence. Right inset: time-resolved PL decay profile below and above the lasing threshold. Reproduced with permission from Ref. [36]. Copyright 2015, American Chemical Society. **(d)** Multimode lasing spectra from a single solution-processed square CH₃NH₃PbClBr₂ microdisk with width of 6.2 μm. Insets: integrated PL intensities as a function of pump fluence, and an emission image of the microdisk above lasing threshold. Reproduced with permission from Ref. [122]. Copyright 2015, Wiley-VCH. **(e)** Optical image (left) and middle (below the lasing threshold) and right (above the threshold) emission images of single solution-processed perovskite NW (scale bar, 10 μm). **(f)** Lasing spectra from single-crystal NW lasers of mixed lead halide perovskites. (e,f) Reproduced with permission from Ref. [3]. Copyright 2015, Nature Publishing Group. **(g)** The evolution from spontaneous emission to lasing in a typical vapor-phase-synthesized CH₃NH₃PbI₃ nanowire. Inset is integrated PL intensities and the FWHM as a function of pumping fluence. **(h)** The bright field image of a single CH₃NH₃PbI₃ nanowire and the corresponding PL images with increasing the pump fluences. (g,h) Reproduced with permission from Ref. [71]. Copyright 2015, American Chemical Society.

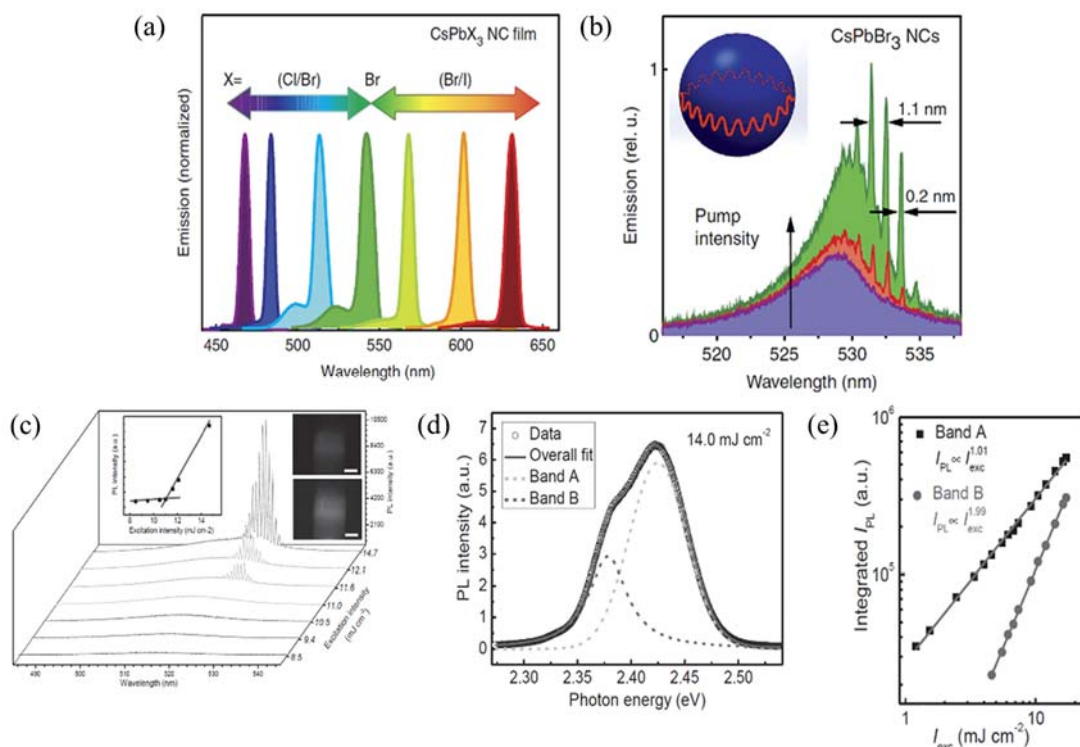


Figure 21. ASE/lasing from colloidal all-inorganic perovskite NPs. **(a)** ASE spectra tuning via compositional modulation. **(b)** Evolution from spontaneous to WGM lasing with increasing pump intensity in a CsPbBr₃ NPs film coated microsphere resonator of 15 μm in diameter. (a-b) Reproduced with permission from Ref. [129]. Copyright 2015, Nature Publishing Group. **(c)** Pump intensity-dependent PL spectra from a CsPbBr₃ NPs infiltrated capillary tube with inner diameter of ~50 μm. The left inset displays the pump fluence dependent integrated PL intensities. The right insets shows the optical images of the NPs infiltrated capillary tube below (upper image) and above (lower image) the lasing threshold (scale bar is 20 μm). **(d)** Fitted PL spectrum with two emission bands at high pump fluence. **(e)** Spectrally integrated PL intensity of two fitted emission bands as a function of excitation intensity. (c-e) Reproduced with permission from Ref. [127]. Copyright 2015, Wiley-VCH.

Table 1. Overview of selected representative results of light-emission from organic-inorganic and all-inorganic halide perovskite in LEDs.

Perovskite Emitter ^[a]	Morphology	Device Architecture ^{[b][c]}	EQE [%]	CE [Cd A ⁻¹]	L _{max} [Cd m ⁻²]	V _T [V]	Publication Date
CH ₃ NH ₃ PbBr ₃ ^[5]	Thin film	ITO/PEDOT:PSS/Pe/F8/Ca/Ag	0.1	0.3	364	3.3	2014-08
CH ₃ NH ₃ PbBr ₃ ^[102]	Thin film	ITO/Buf-HIL/Pe/TPBI/LiF/Al	0.125	0.57	417	~4	2014-11
CH ₃ NH ₃ PbBr ₃ ^[149]	Thin film	ITO/PEDOT:PSS/TPD/Pe/Ag	6.5·10 ⁻³	~1.8·10 ⁻²	21	~4	2015-01
CH ₃ NH ₃ PbI _{3-x} Br _x ^[149] (red)	Thin film	ITO/PEDOT:PSS/TPD/Pe/Ag	1.1·10 ⁻³	n.r. ^[d]	n.r.	n.r.	2015-01
CH ₃ NH ₃ PbBr ₃ ^[101]	Thin film	ITO/PEDOT:PSS/Pe/ZnO/Ca/Ag	n.r.	~21	~550	2	2015-01
CH ₃ NH ₃ PbBr ₃ ^[38]	Thin film	ITO/PEDOT:PSS/Pe-PIP/F8/Ca/Ag	1.2	n.r.	~200	n.r.	2015-02
CH ₃ NH ₃ PbBr ₃ ^[100]	Thin film	ITO/ZnO-PEI/Pe/TFB/MoO _x /Au	0.8	n.r.	~20000	2.8	2015-04
CH ₃ NH ₃ PbI _{3-x} Cl _x ^[100] (red)	Thin film	ITO/ZnO-PEI/Pe/TFB/MoO _x /Au	3.5	n.r.	n.r.	2.2	2015-04
CH ₃ NH ₃ PbBr _{3-x} Cl _x ^[4] (red)	Thin film	FTO/TiO ₂ /Pe/Spiro-MeTAD/Au	0.48	n.r.	n.r.	~1.5	2015-05
CH ₃ NH ₃ PbBr ₃ ^[99]	Thin film	ITO/c-TiO ₂ /EA/Pe/SPB-02T/MoO ₃ /Au	0.051	0.22	~545	n.r.	2015-05
CH ₃ NH ₃ PbBr _{3-x} Cl _x ^[74]	Thin film	ITO/Mg-ZnO/Pe/CBP/MoO _x /Au	0.1	n.r.	n.r.	2.2	2015-07
CH ₃ NH ₃ PbBr ₃ ^[39]	Thin film	ITO/Pe-PEO/In-Ga	0.083	0.38	4,064	2.9	2015-08
CsPbBr ₃ ^[133]	QD	ITO/PEDOT:PSS/PVK/Pe/TPBI/LiF-Al	0.12	0.43	946	4.2	2015-10
CsPbBr ₃ ^[32]	Thin film	ITO/PEDOT:PSS/Pe/F8/Ca/Ag	0.008	0.035	407	3	2015-10
CH ₃ NH ₃ PbBr ₃ ^[104]	Thin film	ITO/PEDOT:PSS/Pe/SPB-02T/LiF/Ag	0.1	0.43	3,490	~2.4	2015-11
CH ₃ NH ₃ PbBr ₃ ^[87]	NPLs	ITO/PEDOT:PSS/Pe/PVK:PBD/BCP/LiF/Al	0.48	n.r.	10,590	3.8	2015-11
CH ₃ NH ₃ PbBr ₃ ^[150]	Thin film	ITO/PEDOT:PSS/Pe (6% HBr)/SPB-02T/LiF/Ag	0.2	0.43	3,490	4.3	2015-11
CH ₃ NH ₃ PbBr ₃ ^[40]	Thin film	Glass/SOCP/Pe/TPBI/LiF-Al	8.53	42.9	~15,000	~4	2015-12
CH ₃ NH ₃ PbBr ₃ ^[105]	Thin film (printed)	ITO/Pe-PEO/Ag NWs	1.1	4.91	21,014	2.6	2015-12

^[a] All perovskites display green emission unless stated differently.

^[b] Pe = perovskite.

^[c] **ITO** = In-doped SnO₂; **PEDOT:PSS** = poly(3,4-ethylenedioxythiophene):polystyrene sulfonate; **F8** = poly(9,9-dioctylfluorene); **Buf-HIL** = buffered hole-injection layer; **TPBI** = 2,2',2''-(1,3,5-benzinetriyl)-tris(1-phenyl-1-H-benzimidazole); **TPD** = *N,N'*-bis(3-methylphenyl)-*N,N'*-diphenylbenzidine); **PIP** = poly(imide) polymer; **PEI** = poly(ethylenimine), **TFB** = poly(9,9-dioctyl-fluorene-co-*N*-(4-butylphenyl)diphenylamine); **EA** = ethanolamine; **SPB-02T** = blue copolymer, Merck Co.; **BCP** = bathocuproine; **PEO** = poly(ethyleneoxide); **PVK** = poly(9-vinylcarbazole); **PVK:PBD** = (poly(9-vinylcarbazole):2-(4-biphenyl)-5-phenyl-1,3,4-oxadiazole), and **BCP** = bathocuproine.

^[d] Not reported.

Table 2. Selected representative results of ASE/lasing from organic-inorganic and all-inorganic halide perovskite gain media.

Material (X= Cl ⁻ , Br ⁻ , or I ⁻)	Morphology	Pump Source	S.E. wavelengths [nm]	Modal gain coefficient [cm ⁻¹]	Threshold (ASE or Lasing) [μJ cm ⁻²]	Cavity Type	Publication Date
CH ₃ NH ₃ PbX ₃ ^[2]	Thin film	600 nm, 150 fs	~500–790	40	~12 (ASE)	N.A.	2014-03
CH ₃ NH ₃ PbI ₃ ^[120]	Thin film	530 nm, 4 ns	~780	-	~10 (ASE)	N.A.	2015-08
CH ₃ NH ₃ PbI _{3-x} Cl _x ^[31]	Thin film	532 nm, 400 ps	~760	-	~120 (ASE) ~0.2 μJ per pulse (lasing)	N.A. Vertical microcavity	2014-04 “
CH ₃ NH ₃ PbI ₃ ^[151]	Thin film	355 nm, 2 ns	~775	~125	~65 (ASE) ~75 (lasing)	N.A. Spherical WGM	2014-10 “
CH ₃ NH ₃ PbI ₃ ^[121]	Thin film	532, 1 ns	~780	-	~0.32 (lasing)	DFB	2015-12
CH ₃ NH ₃ PbBr ₃ ^[122]	Square microdisk	400 nm, 120fs	~550	-	~4 (lasing)	Planar WGM	2015-04
CH ₃ NH ₃ PbI _{3-x} X _x ^[36]	Microplatelet	400 nm, 50fs	~760	-	~40 (lasing)	Planar WGM	2014-08
CH ₃ NH ₃ PbI ₃ ^[152]	Microcrystal networks	355 nm, 0.8 ns	~ 765	-	~200 (lasing)	Random lasing	2014-10
CH ₃ NH ₃ PbX ₃ ^[3]	NWs	402 nm, 150 fs	~500–780	-	~0.2 (lasing)	Fabry-Perot cavity	2015-03
CsPbX ₃ ^[127]	NPs	400 nm, 100fs	~470–620	~98	~22 (ASE) ~11·10 ³ (lasing)	N.A. Ring WGM	2015-10 “
CsPbX ₃ ^[129]	NPs	400 nm, 100fs	~470–640	~450	~5–22 (ASE) N.A. (lasing)	N.A. Spherical WGM / Random lasing	2015-07 “
CsPbBr ₃ ^[128]	NPs	800 nm, 35fs	~520	-	~12·10 ³ (ASE)	N.A.	2015-12
CsPbBr ₃ ^[153]	NWs	400 nm, 150 fs	~530	-	~10 (lasing)	Fabry-Perot cavity	2016-02

Sjoerd A. Veldhuis obtained his Ph.D. in inorganic materials science from MESA+ Institute for Nanotechnology, at the University of Twente (The Netherlands) in 2015. During this period he studied in-depth the formation of inorganic nanomaterials from wet-chemical synthesis routes. He currently works as a research fellow at the Energy Research Institute at Nanyang Technological University (ERI@N) in Singapore. His current research focuses on fabrication of nanostructured materials for light-emission and energy applications.



Pablo P. Boix received his Ph.D. from the Universitat Jaume I (2012, Castelló, Spain). During this period, he analyzed the physical processes of optoelectrical devices including DSC, QDSC, organic solar cells and water splitting systems by impedance spectroscopy. In 2012 he joined the Energy Research Institute at Nanyang Technological University (ERI@N), where his research focuses on the development of perovskite photovoltaic and light-emitting devices, elucidating the working mechanisms which determine their performance.



Subodh G. Mhaisalkar is the Tan Chin Tuan Centennial Professor in the School of Materials Science & Engineering at the Nanyang Technological University (NTU), Singapore. Subodh is also the Executive Director of the Energy Research Institute at NTU (ERI@N), a pan-University multidisciplinary research institute for innovative energy solutions. Prior to joining NTU in 2001, Subodh has over 10 years of research and engineering experience in the microelectronics industry. Subodh received his Bachelors' degree from IIT-Bombay and his MS/Ph.D. degrees from The Ohio State University.

